AmMin7996 Revision2

Formation process of Al-rich calcium amphibole in quartz-bearing eclogites from the Sulu belt, China

MASAKI ENAMI[1, *], TOMOKI TAGUCHI[2, **], YUI KOUKETSU[3], KATSUYOSHI MICHIBAYASHI[3], AND TADAO NISHIYAMA[4]

[1] Institute for Space–Earth Environmental Research, Nagoya University, Nagoya 464-8601, Japan

[2] Department of Geology and Mineralogy, Graduate School of Science, Kyoto University, Kyoto 606-8502, Japan

[3] Department of Earth and Planetary Sciences, Graduate School of Environmental Studies, Nagoya University, Nagoya 464-8601, Japan

[4] Graduate School of Science and Technology, Kumamoto University, Kumamoto 860-8555, Japan

* E-mail: enami@nagoya-u.jp

** Present address: Department of Earth Sciences, School of Education, Waseda University, Shinjuku-ku, Tokyo 169−8050, Japan

ABSTRACT

Aluminum-rich and Si-poor calcium amphibole [~3.9 Al atom per formula unit (apfu) and ~5.5 Si apfu for 23 O] occurs in the quartz-bearing eclogites from the Donghai area, Sulu ultrahigh-pressure metamorphic belt, eastern China. Most of the aluminous

amphibole phases are retrograde products from the exhumation and hydration stage, and are texturally divided into a mantle phase around a porphyroblastic garnet and crack-filling (vein) phase of a garnet. Less aluminous amphibole occurs as symplectite phase with plagioclase after omphacite. The formation process of the aluminous amphibole in the quartz-bearing samples is discussed on the basis of the analytical data by EPMA, FIB-TEM, and EBSD.

The mantle amphibole occurs between garnet and symplectite or quartz. A set of plagioclase and aegirine-diopside/argirine-hedenbergite thin monomineralic bands forms at the boundary between the mantle amphibole and matrix quartz. However, these monomineralic bands do not occur at the mantle amphibole-symplectite boundary. These textural differences indicate that the recrystallization of the aluminous amphibole around garnet was controlled by significant local reactions and the size of equilibrate domains were probably several tens of micrometers or less.

The mantle amphibole is composed of inner (garnet-side) and outer (matrix-side) zones. The inner zone is compositionally homogeneous and its atomic Al/Si value is approximately 0.63–0.66, and similar to that of garnet. Atomic Ca/Si value in the inner zone is also almost uniform, and is generally identical to that of garnet. The outer zone exhibits a monotonic decrease in the Al/Si and Ca/Si values outwards, and its composition at the outermost margin is similar to that of the symplectitic amphibole. The crack-filling amphibole has a composition similar to the inner zone of the mantle amphibole. The CPO pattern of the crack-filling amphibole is different from that of the adjacent mantle amphibole, showing that the crack-filling amphibole is cut by the mantle amphibole. The textural relationship between the mantle and crack-filling amphibole phases and their compositional characteristics imply that (1) the mantle type is a slightly

later stage product than the crack-filling type and (2) the boundary between the inner and outer zones of the mantle aluminous amphibole probably corresponds to the initial surface of the porphyroblastic garnet. The inner zone is considered to have grown inward by simple substitution of garnet, using the tetrahedral and octahedral cations of the garnet as the basic framework. On the other hand, most of the outer zone of the mantle-type amphibole grew outwards in the matrix from the initial surface of the garnet porphyroblast. The mantle amphibole shows a CPO similar to that of amphibole in the adjacent symplectite domain, suggesting that these two types of amphibole formed almost simultaneously, sharing crystallographic orientation with each other.

The formation of crack-filling aluminous amphibole was probably promoted by the hydraulic microfracturing process at an early stage of exhumation and hydration. The mantle and symplectitic amphibole phases formation was promoted by the subsequent infiltration of metamorphic fluid. The aluminous amphibole in the SiO_2 phase-bearing eclogites probably recrystallized with the formation of a localized SiO_2-undersaturated reaction domain because of rapid exhumation and subsequent rapid cooling of the Sulu UHP metamorphic belt.

Keywords: Aluminous amphibole, EPMA, FIB-TEM, EBSD, eclogite, Sulu UHP metamorphic belt

INTRODUCTION

Detailed compilations of the chemical compositions of amphibole formed under various environmental conditions show that most of the calcium amphibole phases are more siliceous and/or less aluminous than the tschermakite–pargasite solid solution (e.g., Deer et al., 1997; Martin, 2007; Schumacher, 2007). An aluminous [~4.5 atom per

formula unit (apfu) for 23O) and Si-poor (~4.6 apfu) calcium amphibole, a sadanagaite, was first reported from spinel-bearing skarns in the Ryoke low pressure (P)/temperature (T) metamorphic belt, Japan, by Shimazaki et al. (1984). Subsequently, the aluminous and Si-poor amphibole, which is hereafter defined as aluminous amphibole unless otherwise stated, has been described from various types of lithologies. They have mostly SiO_2-depleted whole-rock compositions such as metacarbonate (Mogessie et al., 1986), the reaction zone between the crystalline limestone and K-metasomatized basalt in granitic contact aureole (Sawaki, 1989), calc-silicate pods in layered gneisses of the transitional amphibolite and granulite facies conditions (Shiraishi et al., 1994), corundum- and spinel-bearing schist (Savel'eva and Korikovskii, 1998), and K-metasomatized basalt around granite intrusions (Banno et al., 2004). Appleyard (1975) also reported aluminous amphibole (~3.3 Al apfu and ~5.3 Si apfu) from spinel-bearing metasomatic alkaline gneisses before the application for registration and its acceptance as a new mineral, "sadanagaite". The extent of tschermak substitution in calcic amphibole is sensitive to silica activity (e.g., Hoschek, 1995), and these limited occurrences of aluminous calcium amphibole could indicate that the SiO_2-undersaturated system generally plays a definitive role in the formation of aluminous amphibole.

However, Si-poor and aluminous amphibole phases (~3.5–3.7 Al apfu and ~5.8–5.5 Si apfu) have been occasionally reported from retrograde eclogites in Alps (e.g., Mogessie et al., 1986; Messiga et al., 1991; Poli, 1991) and Himalaya (e.g., Palin et al., 2014; O'Brien, 2019). They sometimes occur as pseudomorphs after garnet also in coesite eclogites from several localities of the Sulu ultrahigh-pressure (UHP) metamorphic belt, China, such as Rongcheng, Yangkou, and Donghai areas (~3.5 Al apfu and ~5.5 Si apfu: Enami et al., 1993; Yang, 2004; Liu et al., 2009; Yamasaki et al., 2018). Yang (2004)

discussed the mass transfer during the formation of retrograde amphibole grains using the isocon method. However, it has not been well understood why these aluminous amphibole phases recrystallized in the SiO_2-excess whole-rock compositions.

In this study, we focused on the fact that aluminous amphibole phases, which coexist with coesite/quartz, characteristically occur in eclogites, and systematically analyzed the aluminous amphibole phases in coesite eclogites from the Donghai area of the Sulu UHP metamorphic belt as a case study. We will describe the mode of occurrence, compositional characteristics, and relationships of crystallographic orientations of the aluminous amphibole based on the analytical results of electron probe microanalyzer (EPMA), focused ion beam system (FIB)-transmission electron microscope (TEM), and electron back scattered diffraction (EBSD) method, and then discuss the cause of the formation of aluminous amphibole in SiO_2-saturated rocks.

GEOLOGICAL SETTING AND PETROGRAPHY

Samples studied were collected from Qinglongshan (JDQ03) and Caihu (91CHXX and 91CH08) areas in the Donghai region, which is located at the southwestern part of the Sulu UHP metamorphic belt, eastern China (Fig. 1). Geological map of the Qinglongshan area was reported by Yang (2004). Eclogites (e.g., Zhang et al., 1995; Nagasaki and Enami, 1998), ultramafic and related rocks (e.g., Enami and Zang, 1988; Zhang et al., 2004, 2008, 2011), and their host orthogneiss and paragneiss occur extensively in the Donghai area (Fig. 1b). Hirajima et al. (1990) described a coesite eclogite from Mengzhong, which was one of the first reports of authentic evidence for UHP metamorphism in the Sulu UHP metamorphic belt (Fig. 1b). Many petrological and mineralogical studies have been conducted also on core samples from the Chinese

Continental Scientific Drilling (CCSD) main drill hole (e.g., Liu et al., 2001; Zhang et al., 2006).

Common occurrences of coesite and other UHP index phases indicate that the eclogite, ultramafic rock, and their host gneisses in the Donghai area were extensively recrystallized under the coesite eclogite facies conditions (e.g., Zhang et al., 2005, 2009; Liu and Liou, 2011). Peak metamorphic conditions for the Donghai area were estimated at 2.2–4.0 GPa/620–880 °C (e.g., Zhang et al., 2000; Li et al., 2011; Yamasaki et al., 2018). Yamasaki et al. (2018) systematically studied amphibole-bearing samples from Qinglongshan and Jianchang (Fig. 1b) and concluded that sodium-calcium amphibole phases (barroisite–taramite) have been stable under UHP metamorphic stage. The eclogites in the Donghai area are considered to have experienced near isothermal decompression down to amphibolite or lower-granulite facies conditions during early exhumation (e.g., Enami et al., 1993; Zhang et al., 1995). Mafic phases of the eclogite facies stage were replaced to varying degrees by amphibole and other phases because of hydration reactions undergone during this stage.

Petrographical characteristics of the sample JDQ03 were briefly described by Enami et al. (1993). The present study was conducted on a newly prepared thin section, which contains garnet, amphibole, epidote, phengite, and quartz (former coesite) as the main coesite eclogite facies phases (Fig. 2a). Omphacite grains were completely recrystallized to a symplectitic fine aggregate of sodic diopside, amphibole, and plagioclase. The amphibole of the UHP metamorphic stage was confirmed to occur as inclusions in garnet and matrix phase. Retrogressive amphibole was observed as a zone around garnet (denoted as mantle amphibole hereafter, unless otherwise stated) and symplectitic particles with sodic diopside and plagioclase after omphacite. The segment of mantle

amphibole is composed of a single phase and does not include any other phases. Rutile and apatite are minor constituents, and K-feldspar occurs as an inclusion in garnet. Biotite occurs as a retrograde phase replacing phengite.

The samples 91CHXX and 91CH08 are petrographically similar to each other. They are mainly composed of garnet, amphibole, zoisite/epidote, paragonite, and quartz (former coesite), with accessory minerals rutile and apatite. Omphacite occurs as inclusions in garnet of 91CH08, and matrix omphacite grains of 91CHXX and 91CH08 were completely replaced by symplectite of sodic diopside, plagioclase, and amphibole (Fig. 2b-d). In 91CHXX, amphibole of the eclogite facies stage was confirmed as an inclusion in garnet and in an isolated matrix phase. Retrograde amphibole occurs as crack-filling (vein) phase of garnet other than the mantle and symplectite amphibole phases. The mantle and crack-filling amphibole phases in 91CHXX are a single phase similar to the mantle amphibole in JDQ03 and do not contain any other phases. On the other hand, the mantle and crack-filling amphibole phases in 91CH08 contain fined-grained garnet (less than 25 μm in size).

ANALYTICAL PROCEDURES

The mineral compositions were analyzed using an EPMA with wavelength-dispersive system (WDS, JXA-8900R; JEOL) at the Petrology Laboratory of Nagoya University. The operating conditions were 15 kV accelerating voltage, 12 nA beam current, and a 2–3 μm beam spot diameter. Well-characterized natural and synthetic phases, including synthetic F-phlogopite (F = 8.7 wt%) and natural Cl-rich hastingsite (Cl = 3.27 wt%, Suwa et al. 1987), were employed as standards. Detection limits (2σ level) of F and Cl are 0.03 wt% and 0.01 wt%, respectively. The correction factors calculated by Kato (2005)

were employed for the matrix correction. Representative analyses of amphibole are presented in Table 1. Minerals and endmember abbreviations are from Whitney and Evans (2010), unless otherwise noted.

An ultra-thin section across a garnet–amphibole boundary was made using a FIB system (Helios NanoLab G3 CX, ThermoFisher Scientific) at the Mineralogical Laboratory of Kyoto University. A predefined area (~30 μm^2) was coated with platinum (Pt) and its surround was cut out to a depth of 15 μm using a gallium (Ga) ion beam. Next, the resulting foil was picked up by an *in-situ* tungsten (W)-probe inside the FIB and mounted on a copper (Cu) TEM grid. The extracted sample was thinned to 200 nm using a Ga ion beam at 30 kV with beam currents ranging from 0.1–3 nA and at 5 kV with a beam current of 16 pA for the final processing. The TEM foil was examined at Kyoto University using a TEM (JEM-2100F, JEOL) equipped with an energy-dispersive X-ray spectroscopy (EDS) system (JED-2300T, JEOL) operating at 200 kV. The TEM images were recorded using a charge-coupled device (CCD) camera (Orius200D, Gatan, Pleasanton, CA, USA). The zone axes of individual amphibole and garnet grains were identified based on selected area electron diffraction (SAED) patterns, which were analyzed using a Gatan Digital Micrograph (GMS 3) and the ReciPro software (http://pmsl.planet.sci.kobe-u.ac.jp/~seto/).

Crystal–preferred orientations (CPO) of minerals were measured by indexing EBSD patterns produced in a Hitachi S–3400 N scanning electron microscope equipped with an Oxford AZtec EBSD system at the Petrology Laboratory of Nagoya University. Diffraction pattern acquisition was performed using an acceleration voltage of 20 kV and a working distance of 27 mm. Processing and indexation of Kikuchi bands and post-acquisition processing of crystallographic orientation measurements were made

using HKL Channel 5 software (Oxford Instruments). Pole figures were prepared using PFctf and ROTctf4 computer programs by D. Mainprice and Matlab MTEX toolbox by K. Michibayashi.

MINERALOGY

Amphibole

Amphibole phases are texturally grouped into inclusion in garnet, the matrix phase, symplectite phase, mantle phase, and vein-filling phase of garnet (Fig. 2 and Table 1). Figure 3 compares chemical compositions among these texturally discerned amphibole groups. The Fe^{3+}/Fe^{2+} value of amphiboles was estimated according to the method proposed by Hawthorne et al. (2012) using ACES_9-8.xlsx provided by Locock (2014). Hawthorne et al. (2012) proposed the $^{C}(Al + Fe^{3+} + Cr + 2Ti)–\ ^{A}(Na + K)$ diagram as a criterion for classifying the calcium amphibole, where superscript C and A indicate octahedral site and the largest 10 to 12-coordinated site, respectively. However, the parameter $^{C}(Al + Fe^{3+} + Cr +2Ti)$ also depends on the amount of the substitution $^{B}Na^{C}(Al, Fe^{3+})Ca_{-1}(Mg, Fe^{2+})_{-1}$ in addition to the $^{C}(Al, Fe^{3+})^{T}Al(Mg, Fe^{2+})_{-1}Si_{-1}$ substitution, where superscripts B and T indicate 8-coordinated site and tetrahedral site, respectively. This point should be considered when discussing the chemical compositions of calcium and sodium-calcium amphibole groups in eclogites and their hydrated lithologies. Therefore, the chemical composition of amphibole will be described by adopting the $Si–^{B}Na$ diagram in addition to $^{C}(Al + Fe^{3+} + Cr + 2Ti)–\ ^{A}(Na + K)$ diagram.

Eclogite facies amphibole: The inclusion and matrix amphibole phases show a relatively wide compositional range from sadanagaite/ferro-sadanagaite–pargasite/ferro-pargasite–taramite/ferro-taramite–katophorite/ferro–katophorite as follows: 5.70–6.51 Si apfu [for 24 (OH, F, Cl, O)], 1.32–1.85 ^{C}(Al + Fe^{3+} + Cr + 2Ti) apfu, 0.20–0.66 ^{B}Na apfu, 0.81–0.99 ^{A}(Na + K) apfu, and 0.32–0.61 X_{Mg} [= Mg (Mg + Fe^{2+})] in JDQ03 (Fig. 3a and b); 5.52–6.15 Si apfu, 1.06–1.85 ^{C}(Al + Fe^{3+} + Cr + 2Ti) apfu, and 0.41–0.54 X_{Mg} in 91CHXX (Fig. 3c and d). In 91CHXX, the inclusion amphibole has higher ^{B}Na (0.11–0.45 apfu) and lower ^{A}(Na + K) (0.83–0.96 apfu) than the matrix amphibole [0.02–0.08 ^{B}Na apfu and 0.90–1.00 ^{A}(Na +K) apfu], unlike those in JDQ03. Inclusion and matrix amphibole in JDQ03 are rich in Cl and reach 1.8 wt% and 2.4 wt%, respectively, and are poor in F, which is mostly below the detection limit. The Cl and F contents of amphibole in 91CHXX and 91CH08 are also mostly below the detection limit, respectively.

Retrograde amphibole: Retrograde amphibole phases occur as the mantle phase around garnet, crack-filling phase of garnet [Amp (G)], and symplectitic aggregates after omphacite [Amp (S)]. The mantle amphibole around garnet is divided into those that occur between the garnet-symplectitic omphacite boundary [Amp (O)] and garnet-quartz boundary [Amp (Q)]. Amp (Q) is separated from the quartz matrix by a set of thin bands (30–60 μm in width) of plagioclase [Amp (Q) side] and aegirine-diopside/aegirine-hedenbergite (simply denoted as aegirine-diopside hereafter) (quartz side) (Figs. 2d, 6a, and 9). Image processing of reaction zone between the garnet–quartz for four grains using ImageJ (ver. 1.53j) gives volume proportions of about 56–63%, 21–28%, and 10–21% for Amp (Q), aegirine-diopside, and plagioclase, respectively. A thin amphibole-poor and plagioclase-rich band (20–30 μm in width)

intervenes between the Amp (O) and symplectite after omphacite (e.g., Figs. 4a and 5a). No other phase was observed at the Amp (G)-garnet interface.

The mantle amphibole phases around garnet [Amp (O) and Amp (Q)] were divided into the garnet-side (inner) and symplectite/quartz-side (outer) zones based on compositional variations (Figs. 4b, 5b, and 6b, c). The inner and outer zones of the Amp (O) are 20–40 μm and 15–20 μm in width, respectively, and those in the Amp (Q) are relatively wider (60–80 μm in width) and narrower (~10 μm in width) than the Amp (O), respectively. The inner garnet-side zones of the Amp (O) and Amp (Q) are compositionally homogeneous and have atomic Al/Si values [0.63 (2)–0.66 (1)] similar to garnet [0.65 (1)], where the standard deviation in parentheses (1σ level) corresponds to the last digit of the average value. Atomic Ca/Si values are also constant in the inner zones, and are almost identical to those of the garnet in JDQ03 and 91CHXX. In the outer zones of the Amp (O) and Amp (Q) , the Al/Si and Mg/Fe^{2+} values decrease and increase toward the margin, respectively. The Ca/Si value also decreases toward the margin in most outer zones. Consequently, the outermost rim of the Amp (O) has similar chemical composition to the Amp (S) in the symplectite (Figs. 4b, 5b and 6b). The Amp (G) (60–200 μm in width) is compositionally homogeneous (Fig. 6d) and has the Al/Si value [0.64 (2)–0.65 (1)] similar to the garnet and inner garnet-side zones of the Amp (O) and Amp (Q).

The Amp (O) in JDQ03 has a wide compositional range and is richer in the edenite component and poorer in the sodic amphibole components than the inclusion phase in garnet and matrix phase: 5.62–6.27 Si apfu, 1.16–1.72 $^{C}(Al + Fe^{3+} + Cr + 2Ti)$ apfu, 0.19–0.40 ^{B}Na apfu, 0.84–1.00 $^{A}(Na + K)$ apfu, and 0.45–0.64 X_{Mg} (Fig. 3a and b). The Amp (O) in 91CHXX is poorer in the $^{A}(Na + K)$ component than the matrix phase and in

264 ^{B}Na component than the inclusion phase in garnet: 5.55–6.17 Si apfu, 1.13–1.67 ^{C}(Al +
265 Fe^{3+} + Cr + 2Ti) apfu, 0.04–0.10 ^{B}Na apfu, 0.83–0.96 ^{A}(Na + K) apfu, and 0.47–0.60 X_{Mg}
266 (Fig. 3c and d). The Amp (O), Amp (Q), and Amp (G) in 91CH08 have a similar
267 compositional range, which is relatively limited compared to those in JDQ03 and
268 91CHXX: 5.50–6.03 Si apfu, 1.64–2.00 ^{C}(Al + Fe^{3+} + Cr + 2Ti) apfu, 0.26–0.75 ^{B}Na apfu,
269 0.88–1.00 ^{A}(Na + K) apfu, and 0.27–0.41 X_{Mg} (Fig. 3e and f).
270 The symplectitic Amp (S) is poorer in the tschermak component and higher in X_{Mg}
271 value than the other amphibole phases (Fig. 3): 5.94–6.73 Si apfu, 0.77–1.41 ^{C}(Al + Fe^{3+}
272 + Cr + 2Ti) apfu, 0.12–0.36 ^{B}Na apfu, 0.77–0.98 ^{A}(Na + K) apfu, and 0.60–0.72 X_{Mg} in
273 JDQ03; 6.03–6.29 Si apfu, 1.04–1.23 ^{C}(Al + Fe^{3+} + Cr + 2Ti) apfu, 0.05–0.10 ^{B}Na apfu,
274 0.81–0.96 ^{A}(Na + K) apfu, and 0.53–0.58 X_{Mg} in 91CHXX; and 5.72–6.15 Si apfu,
275 1.62–1.83 ^{C}(Al + Fe_{3+} + Cr + 2Ti) apfu, 0.39–0.82 ^{B}Na apfu, 0.97–1.00 ^{A}(Na + K) apfu,
276 and 0.44–0.66 X_{Mg} in 91CH08.
277 The Cl and F contents of the retrograde amphibole are mostly below the detection
278 limit.

279 **Garnet and other phases**

280 Garnet porphyroblasts are homogeneous, and there is no distinct compositional
281 modification at the interface with the amphibole. They are a grossular-rich
282 almandine-pyrope series and have end-member proportions, which are calculated
283 assuming total iron as FeO, of $Alm_{48–50}Prp_{21–22}Sps_{1–2}Grs_{28–29}$ in JDQ03,
284 $Alm_{47–50}Prp_{17–19}Sps_{1}Grs_{32–34}$ in 91CHXX, and $Alm_{49–53}Prp_{12–14}Sps_{2–3}Grs_{33–36}$ in 91CH08.
285 Small garnet grains included in the Amp (O) and Amp (G) of 91CH08 are distinctly
286 grossular-richer than the garnet porphyroblasts, and their end-member proportions

calculated on the basis of charge balance and stoichiometry assuming 8 total cation for 12 O (Droop, 1987) are $Alm_{19–32}Prp_{1–3}Sps_{5–8}Grs_{55–68}Adr_{2–8}$.

Clinopyroxene grains are grouped into omphacite included in garnet, sodic diopside in the symplectite, and aegirine-diopside in the Amp (Q)–quartz boundary. Omphacite grains are homogeneous and their compositions calculated based on charge balance and stoichiometry (4 total cation for 6 O) are $Jd_{60–64}Di/Hd_{29–33}Aeg_{6–8}$ and 0.60–0.72 X_{Mg} in 91CH08. Sodic diopside grains are $Jd_{9–28}$ $Di/Hd_{67–78}Aeg_{5–15}$ and 0.80–0.90 X_{Mg}, $Jd_{6–7}$ $Di/Hd_{72–80}Aeg_{14–22}$ and 0.71–0.81 X_{Mg}, and $Jd_{5–24}$ $Di/Hd_{44–51}Aeg_{25-50}$ and 0.60–0.82 X_{Mg} in JDQ03, 91CHXX, and 91CH08, respectively. Aegirine-diopside grains in 91CH08 are $Jd_{2–9}$ $Di/Hd_{35–54}Aeg_{37–62}$ and 0.21–0.59 X_{Mg}.

Anorthite contents of plagioclase grains in the symplectite are $An_{8–16}$, An_{15-18}, and $An_{8–26}$ in JDQ03, 91CHXX, and 91CH08, respectively. Plagioclase grains around the matrix zoisite in 91CH08 are slightly calcic (~ An_{26}). X_{Fe} [= $Fe^{3+}/(Fe^{3+} + Al)$] values of epidote in JDQ03 are 0.23–0.26. In 91CH08, X_{Fe} values of coexisting prograde zoisite and epidote are 0.04–0.05 and 0.10–016, respectively. Some zoisite and epidote grains have SrO up to 1.2 and 2.7 wt%, respectively (Nagasaki and Enami, 1998).

FIB-TEM OBSERVATION

Using the FIB, we cut the selected portion of the interface between the Amp (O) and garnet of 91CHXX. Figure 7 shows the high-angle annular dark-field scanning TEM (HAADF-STEM) and bright field (BF)-TEM images of the investigated TEM foil. The HAADF-STEM (Fig. 7a) and X-ray images show that the Amp (O) and garnet are compositionally homogeneous and their SAED patterns are uniquely consistent with those of calcium amphibole and garnet (Fig. 7a and its insets). The BF-TEM image was

observed from the [001] direction of the Amp (O), and shows that some subgrain boundaries were developed within the Amp (O) in contrast to the garnet (Fig. 7b). The TEM observations show that the interface between the Amp (O) and garnet form sharp boundaries and no other phases crystallized at the interfaces between these two phases.

EBSD ANALYSIS

Amphibole replacing garnet

The Amp (O), Amp (Q), and Amp (G) show characteristic EBSD images, respectively. The Amp (O) is divided into several segments of 600–700 μm or more in length. Each segment has a nearly identical CPO and is probably a single crystal (Figs. 8a and 9). The Amp (Q) is mainly composed of several segments (200–350 μm in length). Each segment is an aggregate of subgrains (less than 50–100 μm in size) that have similar CPO (Fig. 9). The Amp (G) is composed of an aggregate of anhedral and prismatic crystals (20–80 μm in length), which mostly extend toward the center of the vein from the interface with the host garnet on either side (Fig. 9 and 10a).

The Amp (O) and Amp (Q) surround a set of garnet and crack-filling Amp (G) (Figs. 9, 10a, and 11a). Figure 10 shows contrasts of CPO patterns and compositional zoning between the Amp (Q) and Amp (G). In the analyzed part, the Amp (Q) is composed of domains 5 and 6 (Fig. 10a). They are composed of several segments, which have a similar crystallographic orientations, respectively (Fig. 10b). However, the domains 7 of the Amp (G) exhibits weak girdles of orientations in (010) and [001], showing different CPOs to the Amp (Q) (Fig. 10b). These data clearly suggest that the Amp (G) is cut by the Amp (Q). A similar relationship was also observed between the Amp (G) and Amp (O) (right part of Fig. 9 and left-lower part of Fig. 11a). As shown in a compositional zoning

335 through the boundary between the Amp (G) and Amp (Q) (Fig. 10c), part of the Amp (G)
336 was compositionally homogeneous and its Al/Si value [0.65 (1)] is similar to that of the
337 porphyroblastic garnet [0.65 (0)]. In contrast, in the Amp (Q) part, the Al/Si and Ca/Si
338 values decrease and Mg/Fe^{2+} value increases toward the outermost margin and reach 0.51,
339 0.18, and 0.51, respectively.
340

341 **CPO relationship between Amp (O) and Amp (S)**

342 The EBSD mappings of boundaries between the Amp (O) and Amp (S) domains,
343 which are in contact with each other, qualitatively show that these two-types of
344 amphibole share similar CPO patterns (Figs. 8a, 9 and 11a). Figure 11b and c
345 quantitatively compare the CPO patterns of the Amp (O) and Amp (S), which constitute
346 bordering domains. Each set of neighboring Amp (O) and Amp (S) shows a similar CPO
347 pattern; thus, the two Amp (O) domains, which are located on either side of the Amp (S)
348 domain, also share a similar CPO pattern: e.g., sets of domains 8, 9, and 10 (Fig. 11b) and
349 domains 11, 12, and 13 (Fig. 11c). The Amp (O) segment and Amp (S) grains are
350 sometimes continuous at their interface, thus forming a single crystal (cf. the parts
351 enclosed by the circles in Figs. 8a and 11a).
352

353 **CPO relationship between Amp (S) and symplectitic sodic diopside**

354 The CPO data show that the symplectitic sodic diopside grains form a domain structure
355 with the same crystal orientation (Fig. 8b). The ranges of the sodic diopside domain are
356 almost identical to those of the Amp (S) domain, and these two phases share the same
357 orientations of (100), (010), and [001] for each domain (Fig. 8c and d).
358

FORMATION CONDITIONS OF AMPHIBOLE

Symplectite amphibole [Amp (S)] and mantle amphibole around the garnet [Amp (O) and Amp (Q)] closely coexist with plagioclase, suggesting that the assemblage of these two phases formed during the exhumation and hydration stage of the eclogites. The Amp (O) and Amp (Q) are systematically zoned and have minimum Al/Si and Ca/Si values and maximum Mg/Fe^{2+} value at the interface with plagioclase (Figs. 4b, 5b, and 6b, c). Their interface chemical compositions might have represented the final recrystallization of these two phases.

The following net-transfer reactions were proposed for a calcic amphibole-plagioclase geothermometer (Blundy and Holland, 1990; Holland and Blundy, 1994):

$$NaCa_2(Mg, Fe^{2+})_5(AlSi_7)O_{22}(OH)_2 + 4\ SiO_2 = Ca_2(Mg, Fe^{2+})_5Si_8O_{22}(OH)_2 + NaAlSi_3O_8 \quad (R1)$$

$$NaCa_2(Mg, Fe^{2+})_4Al(Al_2Si_6)O_{22}(OH)_2 + 4\ SiO_2 = Ca_2(Mg, Fe^{2+})_4Al(AlSi_7)O_{22}(OH)_2 + NaAlSi_3O_8 \quad (R2)$$

$$NaCa_2(Mg, Fe^{2+})_5(AlSi_7)O_{22}(OH)_2 + NaAlSi_3O_8 = Na(NaCa)(Mg, Fe^{2+})_5Si_8O_{22}(OH)_2 + CaAl_2Si_2O_8 \quad (R3)$$

However, the amphiboles discussed in this paper are significantly rich in the $^{A}(Na + K)$ component, which is usually >0.8–0.9 apfu (Fig. 3), and probably contain little amount of the edenite-free end-member components such as tremolite and hornblende. Therefore, the tremolite- or hornblende-bearing geothermometers [reactions R1and R2] would be inappropriate for estimating the temperature of the aluminous amphibole-bearing equilibrium. Consequently, a combination of the reaction R3 for the geothermometer [thermometer B of Holland and Blundy (1994)] and the Al/Si

partitioning between amphibole and plagioclase for the geobarometer (Molina et al., 2015) was employed for the P-T estimations (Table 2). Compositions of the outermost parts of the Amp (O) and Amp (Q), which contact plagioclase (cf. Figs. 4a–6a), were used for the P/T calculations. On the other hand, average compositions were employed for plagioclase and Amp (S). The pairs of Amp (O)/Amp (Q)/Amp (S) and plagioclase showed similar equilibrium conditions with each other and those of samples are as follows: 0.87 (6)–0.97 (4) GPa/674 (16)–675 (4) °C for JDQ03; 0.83 (2)–0.92 (2) GPa/686 (10)–701 (6) °C for 91CHXX; and 1.28 (18)–1.33 (20) GPa/694 (14)–729 (22) °C for 91CH08, where the number in parentheses indicates the standard deviation (1σ level) (Table 2).

The Donghai eclogites are considered to have experienced nearly isothermal decompression at the beginning of exhumation, and their P/T conditions at peak metamorphic and/or early exhumation stages were estimated at around 3.2–3.6 GPa/680–840 °C (Zhang et al., 1995, 2005; Frezzotti et al., 2007; Li et al., 2011; Curetti et al., 2018; Li et al., 2018). The estimated formation temperatures of the aluminous amphibole-plagioclase pairs are within the range of those reported during UHP metamorphism, and are consistent with the exhumation P-T path of nearly isothermal decompression discussed by many authors (Fig. 12).

DISCUSSION

Stability of aluminous amphibole

Sadanagaite and related aluminous calcium amphibole generally occur in SiO_2-undesaturated lithologies as summarized in Mogessie et al. (1986), Hawthorne and Harlow (2008), and the current study. These limited modes of occurrences might indicate

that the Si-undersaturated system strongly promotes the formation of aluminous amphibole. However, aluminous amphibole phases occasionally occur in retrograde coesite and/or quartz-bearing eclogites as described in this study and reported in additional work, for example, Mogessie et al. (1986). Total Al, ^{C}Al, and Al/Si values of calcium amphibole coexisting with plagioclase systematically increase with increasing pressure, at least up to 1.2–1.5 GPa (Molina et al., 2015); thus, relatively high-pressure conditions might contribute to the stabilization of the aluminous calcium amphibole in plagioclase-bearing assemblage.

Stable amphibole phases of the eclogite facies stage are generally sodium–calcium amphibole of the barroisite–taramite/katophorite series (e.g., Massonne, 2012; Yamasaki et al., 2018). In contrast, aluminous amphibole phases were generally reported as retrograde products (e.g., Palin et al., 2014; Chatterjee and Jagoutz, 2015; O'Brien, 2019), although those with ~5.8 Si apfu and ~3.3 Al apfu were also reported as inclusions in the garnet of eclogites from the Western Gneiss Region (e.g., Medaris et al., 2018). These data likely suggest that relatively high-pressure environments might be a necessary condition, but are not sufficient for the formation of aluminous amphibole in eclogites and their retrograde lithologies.

The aluminous amphibole in the Donghai eclogites exhibits several different textures and compositional zonings, which are key to understanding the origin of aluminous amphibole in the coesite/quartz-bearing eclogites. The mantle amphibole around garnet [Amp (O) and Amp (Q)] and crack-filling amphibole [Amp (G)] exhibit different interface textures that are closely related to the phase they contacted. A set of thin bands of plagioclase and aegirine-diopside develops between the Amp (Q) and quartz (Fig. 6a). However, no other phase was observed at the boundaries between the Amp (O) and

symplectite and between the Amp (G) and garnet (Figs. 4a–6a). The Amp (O) and Amp (Q) consist of the inner garnet-side and outer matrix-side zones, which are compositionally homogeneous and monotonically zoned, respectively (Figs. 4b, 5b, and 6b, c). The Amp (G), on the other hand, is homogeneous and has a chemical composition similar to that of the inner zone of the Amp (O) and Amp (Q). The coexistence of these three types of amphibole was observed to have occurred at the varying parts of a garnet grain (Figs. 6a and 9). These textural and compositional differences suggest that the recrystallizations of aluminous amphibole replacing garnet was controlled by individual reactions that proceeded locally in each domain.

Formation process of amphibole in the Donghai eclogite

Figure 13 shows a possible formation model of the aluminous amphibole in the Donghai eclogites. Although a minor calcium amphibole occurs as inclusions in garnet, and the matrix phase in the eclogite facies and early exhumation stages, the initial major mafic phases were garnet and omphacite (Fig. 13a), which have eventually been replaced by calcium amphibole through subsequent hydration reactions.

Formations of crack-filling and mantle amphiboles: The compositional similarity of the inner zones of the Amp (O) and Amp (Q) to the Amp (G) indicates that these zones are considered to have formed as pseudomorphs after garnet, similarly to the Amp (G). However, the following characteristics could be observed between the Amp (O)/Amp (Q) and Amp (G): (1) The CPO pattern is discontinuous at the boundaries between them (Figs. 10b and 11b, c), and (2) the Amp (G) is texturally cut or partly surrounded by the Amp (O) or Amp (Q) (Figs. 9, 10a, and 11a). These textural characteristics likely

455 suggest that the Amp (G) first replaced garnet along cracks (Fig. 13b), and then the
456 Amp (O)/Amp (Q) formed slightly later. The Amp (G) was probably formed in
457 connection with the hydraulic fracturing process in the early stages of hydration, while
458 the Amp (O) and Amp (Q) were subsequently formed by hydration reactions caused by
459 subsequent grain-boundary processes.

460 Two models of 1 and 2 are assumed for the formation process of the Amp (O) and
461 Amp (Q). Model 1 interprets that: (1) the end of the Amp (G) stretch direction [point X:
462 boundary between the Amp (G) and Amp (Q) of Fig. 10a, c] was an initial surface of a
463 garnet porphyroblast before formation of the Amp (O) and Amp (Q), and (2) the Amp
464 (O) and Amp (Q) have been initially nucleated at the interface between garnet and
465 omphacite/quartz, and then grew to replace the garnet (inward) and symplectite/quartz
466 (outward), respectively (Fig. 13d1). This model suggests that (1) the boundary between
467 the inner and outer zones of Amp (O) and Amp (Q) is almost identical to the initial
468 surface of the garnet porphyroblast (white broken line in Fig. 13d1) and thus, the inner
469 zone is a pseudomorph after garnet and the outer zone occupies the original matrix part.
470 In contrast, model 2, assumes that the Amp (O) and Amp (Q) are pseudomorphs after
471 garnet in their entirety (Fig. 13c), and that their outer zones represent parts whose
472 chemical composition has been modified by later re-equilibration (Fig. 13d2). In this
473 model, the textural relationships between the Amp (G) and Amp (O)/Amp (Q) shown in
474 Figs. 9, 10a, and 11a are explained as a partial resetting of the chemical composition
475 and COP of Amp(G) during the formation of the outer zone. However, this
476 interpretation does not well explain why the chemical composition and CPO of the Amp
477 (G) were not modified at the stage when the Amp (O)/Amp (Q) were initially formed
478 (Fig. 13c). In addition to this issue, the singular value decomposition (SVD) analysis of

479 the reaction zone at the Amp (Q)–Qz boundary indicates that the volume of Amp (Q)
480 formed by the assumed hydration reaction was likely to have been larger than that of the
481 consumed garnet, as described later. Therefore, the model 1 seems to better explain the
482 formation process of the inner and outer zones of mantle amphibole.
483
484 **Formations of Amp (S) and Amp (O):** The amphibole phases in symplectite [Amp
485 (S)] form domains of 300–700 μm in size, in which they share similar crystallographic
486 orientation (Figs. 8a, c and 11). These domains contain sodic diopside particles with
487 similar crystallographic orientation in each domain (Fig. 8b, d). Furthermore, the Amp
488 (S) and sodic diopside characteristically show almost the same CPO pattern in each
489 domain (Fig. 8c, d). The sodic diopside + plagioclase symplectite was considered to
490 have formed by the replacement of omphacite at early exhumation stage, and the Amp
491 (S) was subsequently grown under the strong control by the crystal orientation of the
492 symplectitic sodic diopside with progressive infiltration of metamorphic fluid (Fig.
493 13c).
494 A set of the Amp (O) and Amp (S) in contact shares a similar CPO pattern, and thus,
495 several Amp (O) segments occurring around a symplectite domain all share a common
496 CPO (e.g., set of domains 8 and 9 and set of domains 11 and 12 in Fig. 11). These CPO
497 data indicate that the Amp (S) in symplectite domain served to have linked the
498 crystallographic orientations of the several Amp (O) domains around the symplectite.
499 The recrystallizations of the Amp (O) and Amp (S) likely began almost simultaneously,
500 and the Amp (O) grew in synchronization with the crystallographic orientation of the
501 Amp (S) (Fig. 13c or d1). The Amp (Q) may also have formed at a similar stage as the
502 Amp (O) and Amp (S).

503 The textural and CPO relationships suggest that the (1) sodic diopside + plagioclase
504 symplectite had probably formed before the Amp (S), (2) the Amp (G) formed slightly
505 earlier than the Amp (O) and Amp (Q), and (3) the Amp (O) and Amp (Q) formed at
506 about the same stage as Amp (S). However, it is unclear whether the formation of
507 symplectitic sodic diopside preceded that of the Amp (G), or if these phenomena were
508 nearly simultaneous (Fig 13b). The Amp (G) was probably formed in connection with
509 hydraulic micro-fracturing process in the early stages of hydration, while Amp (O),
510 Amp (Q), and possibly Amp (S) were subsequently formed by hydration reactions
511 caused by grain-boundary processes (e.g., Putnis and Austrheim, 2010).
512
513 **Formation of aluminous calcium amphibole in SiO_2-saturated rocks**
514 The inner zones of the Amp (O) and Amp (Q), which are pseudomorphs after garnet,
515 are compositionally homogeneous and their Al/Si values are significantly similar to
516 those of garnet (Fig. 4b, 5b, and 6b, c). The Al/Si value of the Amp (G) is also similar
517 to that of garnet (Fig. 6d). Additionally, the FIB-TEM and EMPA observations of the
518 amphibole-garnet interface in micro- and nano-scales demonstrated that Amp (O), Amp
519 (Q), and Amp (G) are single phase and contain no other phases. These data may indicate
520 that the inner zone of the Amp (O), Amp (Q), and Amp (G) would grow by simple
521 substitution of garnet, using tetrahedral and octahedral cations (Si and Al) of the garnet
522 as the basic framework.
523 Diffusion coefficients of major elements in amphibole are not well understood.
524 However, in the case of pyroxene, which has similar crystal structure of inosilicates to
525 amphibole, diffusion coefficients of Ca, Al, and Si are one to three orders of magnitude
526 lower than those of Mg and Fe^{2+} (Cherniak and Dimanov, 2010). Considering these

527 diffusion coefficients of pyroxene as a reference, the inner zones of the Amp (O) and
528 Amp (Q) might have been formed by the preferential diffusion of Mg, Fe^{2+}, and alkali
529 elements between garnet and the matrix. Whereas, Si and Al, which have smaller
530 diffusion coefficients, likely did not migrate much, and contributed to the growth of
531 amphibole with little change in their ratio from the garnet value. This process, coupled
532 with hydration and a significantly local reaction, may have allowed the formation of
533 aluminous calcium amphibole in the quartz-bearing eclogites from the Donghai area,
534 Sulu UHP metamorphic belt.

535 In JDQ03 and 91CHXX, the Ca/Si values of the aluminous amphibole are also
536 similar to those of garnet (Figs. 4b and 5b). Calcium, in addition to Si and Al, did not
537 diffuse much during the inner zone growth in these samples. The Ca/Si value of the
538 aluminous amphibole in 91CH08 are lower than those of garnet (Fig. 6a, b, c), unlike
539 JDQ03 and 91CHXX. The garnet grains in 91CH08 are richer in the Grs component
540 [34.9 (1.0) mol.%] than those in JDQ03 [27.5 (1.8) mol%] and 91CHXX [33.0 (0.5)
541 mol%]. Therefore, small Grs-rich garnet grains were nucleated during the hydration stage
542 of garnet, which would have decreased the Ca/Si value of the aluminous amphibole.
543

544 **Numerical examination of mantle amphibole formation:** Textural characteristics
545 suggest that the Amp (Q) with aegirine-diopside and plagioclase at the boundary between
546 garnet and quartz were formed by infiltration of metamorphic fluid dissolving sodium,
547 potassium, and some other elements in the following qualitative reaction:

548 $$Grt + Qz + Na_2O + O_2 + H_2O = Amp\ (Q) + Aeg\text{-}di + Pl \qquad (R4)$$

549 The possibility of deriving the reaction R4 was investigated using the SVD method
550 (Fisher, 1989; Nishiyama et al., 2017) based on the assumption of conservation of SiO_2,

Al_2O_3, and CaO and considering discussions in the previous section. Other components such as FeO, MgO, MnO, $NaO_{1/2}$, $KO_{1/2}$, and H_2O are treated as mobile components. The cation proportions and molar volumes of the minerals in 91CH08 employed for the SVD calculation are listed in Table 3. The volume of the outer zone of Amp (Q) is distinctly smaller than that of the inner zone (cf. Fig. 6c), and thus, the average composition of the inner zone was adopted as the composition of the product Amp (Q) for the calculation. The sample does not contain any Fe-oxide phase, and garnet and quartz assumed as reactants do not contain Fe_2O_3 as a major component. Therefore, in the calculations, Fe_2O_3 contents in the products of Amp (Q) and aegirine-diopside were assumed to not have been supplied from outside the system, instead, primarily by oxidation of FeO in the reactant garnet during the reaction progress.

We constructed a matrix of mineral compositions given in the atomic proportions per formula unit in the system SiO_2-Al_2O_3-CaO as shown by superscript a in Table 3. The SVD of the matrix gives the following two reactions:

$$-0.704\ \mathrm{Grt} - 0.477\ \mathrm{Qz} + 0.416\ \mathrm{Amp} + 0.299\ \mathrm{Aeg\text{-}di} - 0.119\ \mathrm{Pl} = 0 \qquad \text{(R5)}$$

and

$$-0.342\ \mathrm{Grt} + 0.771\ \mathrm{Qz} + 0.314\ \mathrm{Amp} - 0.173\ \mathrm{Aeg\text{-}di} - 0.401\ \mathrm{Pl} = 0. \qquad \text{(R6)}$$

Both the R5 and R6 do not represent the proper reaction relation that explains the texture of Amp (Q) and related phases. However, the linear combination of these two reactions, (R5) – a(R6), can represent the proper reaction relation in some range of the value of parameter $a = \xi_6/\xi_5$, where ξ_5 and ξ_6 represent the reaction extents of R5 and R6, respectively. We get

$$(-0.704 + 0.342a)\ \mathrm{Grt} + (-0.477 - 0.771a)\ \mathrm{Qz} + (0.416 - 0.314a)\ \mathrm{Amp} + (0.299 + 0.173a)\ \mathrm{Aeg\text{-}di} + (-0.119 + 0.401a)\ \mathrm{Pl} = 0 \qquad \text{(R7)}$$

575 The stoichiometric coefficients of minerals give proper signs, positive for products (Amp,
576 Aeg-di, and Pl) and negative for reactants (Grt and Qz), when $0.30 < a < 1.33$.
577 Figure 14 shows the volume changes of minerals based on the calculated
578 stoichiometric coefficients of minerals as functions of the parameter *a* and their molar
579 volumes listed in Table 3. Although the volume of the product amphibole and the reactant
580 garnet both decrease as the parameter *a* increases, the decreasing ratio is greater for the
581 amphibole (Fig. 14a). Thus, when the parameter *a* is less than 0.68, the volume of the
582 product amphibole exceeds that of the consumed garnet, and this relationship is reversed
583 at $a > 0.68$. Figure 14b shows the relationship between parameter *a* and the volume
584 proportions of Amp(Q), aegirine-di, and plagioclase in the reaction zone calculated by
585 SVD method. This figure also indicates the range of parameter *a* that can simulate the
586 volume proportions of these minerals for the four grains in 91CH08 estimated by image
587 processing. As the parameter *a* increases, the Amp (Q) volume proportion in the reaction
588 zone systematically decreases, and those of arginine-diopside and plagioclase increase.
589 Thus, the abundance ratios of amphibole, aegirine-diopside, and plagioclase become
590 similar to each other as the parameter *a* increases, and they become almost equal when the
591 parameter *a* is about 1.0. The estimated volume range of Amp (Q) for four grains
592 (56–63% and 61% in average) gives a relatively narrow range of parameter *a*
593 (0.58–0.69). On the other hand, the ranges of parameter *a* assumed from the volumes of
594 aegirine-diopside (21–28% and 25 % in average) and plagioclase (10–21% and 15 % in
595 average) are 0.34-0.70 and 0.55-0.79, respectively, which are wider than those
596 estimated by Amp (Q). This is due to that the rate of change of volume of
597 aegirine-diopside and plagioclase for parameter a is significantly smaller than that of
598 Amp (Q). Therefore, it would be appropriate to discuss the range of parameter a from

599 the volume estimate of Amp (Q), rather than referring to that of aegirine-diopside and
600 plagioclase (Fig. 14b). The reaction zone seems to be best simulated by assuming that
601 the parameter a is around 0.6. The range of parameter *a* estimated from the average
602 volumes of Amp (Q), aegirine-diopside, and plagioclase is 0.53-0.65, which is almost
603 identical to the value estimated from Amp (Q). These data suggest that the reaction zone
604 probably formed under conditions where the volume of product Amp (Q) was larger
605 than that of consumed garnet. Consequently, the SVD analysis also indicates that the
606 model 1 shown in Fig. 13 is appropriate to explain the formation process of aluminous
607 amphibole.
608 Stoichiometric coefficients of mobile components are also calculated by combining the
609 stoichiometric coefficients of minerals and the mineral compositions (Fig. 14c). The
610 conspicuous feature is that all mobile components are added from the exterior to form the
611 Amp (Q) – (Aeg-di) - Pl reaction zone. The results by SVD analysis suggest that under
612 certain conditions with infiltration of the metamorphic fluid, the R4 reaction can
613 proceed to form the mineral combination observed in 91CH08.
614

615 **IMPLICATIONS**

616 The formation process of retrograde amphiboles replacing garnet in the Donghai
617 eclogites strongly depends on the mineral phases in contact with the garnet, and is an
618 extremely local phenomenon. The range of chemical equilibrium was narrow and
619 probably less than several tens of micrometers in size. Hacker et al. (2009) compiled
620 chronological data of their new analyses and those published in literature, and pointed out
621 the rapid exhumation of Sulu UHP terrane to a crustal level (0.5–2.5 cm/yr) and a
622 relatively short duration of subsequent amphibolite facies metamorphism with rapid

623 cooling (50–200 °C/Myr). Liu and Liou (2011) estimated the exhumation rate of the
624 Dabie-Sulu UHP metamorphic belt as 0.5 –1.13 cm/yr based on the U-Pb SHRIMP ages
625 of zircon grains. Taguchi et al. (2018) reported the amorphous SiO_2 phase containing
626 nanocrystalline quartz in pseudomorphs after coesite from the Yangzhuang area near the
627 Donghai area, and suggested a rapid cooling during amphibolite facies and subsequent
628 stages. These rapid cooling processes might have maintained a very local and limited
629 element transfer and advanced the crystallization of aluminous amphiboles in the
630 Donghai eclogites.
631 The rapid exhumation and cooling of HP-UHP eclogites were also reported from
632 other continent-continent collision zones, such as the Alps metamorphic region (1.6–3.4
633 and >3.6 cm/yr and 85–100 °C/Myr: e.g.,Gebauer et al., 1997; Rubatto and Hermann,
634 2001; Glodny et al., 2005) and Kokchetav Massif, Kazakhstan (several
635 millimeters–several centimeters/yr: e.g., Katayama et al., 2001; Hacker et al., 2003;
636 Dobretsov and Shatsky, 2004). Aluminous amphibole pseudomorphs after garnet, which
637 show texture similar to the case of the Donghai eclogite, were reported from retrograde
638 eclogites in Central Oetztal, the eastern Alps (Mogessie et al., 1986) and Tso Morari
639 Massif, Himalaya (e.g., Palin et al., 2014; Chatterjee and Jagoutz, 2015). The aluminous
640 calcium amphiboles might have widely formed during rapid exhumation as a retrograde
641 product even in SiO_2-saturated eclogites, especially as a pseudomorph after garnet.
642

643 **ACKNOWLEDGEMENTS AND FUNDING**

644 We would like to thank A. Miyake and Y. Igami for their help with the FIB-TEM
645 analysis, D. Mainprice for providing the original software to analyze the CPO data. The
646 constructive comments by D. Waters, an anonymous reviewer, and handling editor D.

647 Dolejš were helpful in improving the manuscript. The study samples from Caihu were
648 collected as a part of a co-operative project among Kyoto University, Nagoya
649 University, Kanazawa University, and the Institute of Geology, Academia Sinica in
650 1991. This research was partially supported by JSPS KAKENHI Grant Number,
651 JP17K05705 to M.E.
652

REFERENCES CITED

Appleyard, E.C. (1975) Silica-poor hastingsitic amphiboles from metasomatic alkaline gneisses at Wolfe, eastern Ontario. Canadian Mineralogist, 13, 342-351.

Banno, Y., Miyawaki, R., Matsubara, S., Makino, K., Bunno, M., Yamada, S., and Kamiya, T. (2004) Magnesiosadanagaite, a new member of the amphibole group from Kasuga-mura, Gifu Prefecture, central Japan. European Journal of Mineralogy, 16, 177-183.

Blundy, J.D., and Holland, T.J.B. (1990) Calcic amphibole equilibria and a new amphibole plagioclase geothermometer. Contributions to Mineralogy and Petrology, 104, 208-224.

Chatterjee, N., and Jagoutz, O. (2015) Exhumation of the UHP Tso Morari eclogite as a diapir rising through the mantle wedge. Contributions to Mineralogy and Petrology, 169, 3.

Cherniak, D.J., and Dimanov, A. (2010) Diffusion in pyroxene, mica and amphibole. Reviews in Mineralogy and Geochemistry, 72, 641–690.

Curetti, N., Bonadiman, C., Compagnoni, R., Nodari, L., Corazzari, I., and Pavese, A. (2018) Phengite megacryst quasi-exsolving phlogopite, from Sulu ultra-high pressure metamorphic terrane, Qinglongshan, Donghai County (eastern China): New data for P-T-X conditions during exhumation. Lithos, 314, 156-164.

Deer, W.A., Howie, R.A., and Zussman, J. (1997) Double-Chain Silicates. 764 p. The Geological Society, London.

Dobretsov, N.L., and Shatsky, V.S. (2004) Exhumation of high-pressure rocks of the Kokchetav Massif; facts and models. Lithos, 78, 307-318.

677 Droop, G.T.R. (1987) A general equation for estimating Fe^{3+} concentrations in
678 ferromagnesian silicates and oxides from microprobe analyses, using
679 stoichiometric criteria. Mineralogical Magazine, 51, 431-435.
680 Enami, M., and Zang, Q. (1988) Magnesian staurolite in garnet-corundum rocks and
681 eclogite from the Donghai district, Jiangsu province, east China. American
682 Mineralogist, 73, 48–56.
683 Enami, M., Zang, Q., and Yin, Y. (1993) High-pressure eclogites in northern
684 Jiangsu-southern Shandong province, eastern China. Journal of Metamorphic
685 Geology, 11, 589-603.
686 Ferrando, S., Frezzotti, M.L., Dallai, L., and Compagnoni, R. (2005) Fluid-rock
687 interaction in UHP phengite-kyanite-epidote eclogite from the Sulu Orogen,
688 eastern China. International Geology Review, 47, 750-774.
689 Fisher, G.W. (1989) Matrix analysis of metamorphic mineral assemblages and
690 reactions. Contributions to Mineralogy and Petrology, 102, 69–77.
691 Frezzotti, M.L., Ferrando, S., Dallai, L., and Compagnoni, R. (2007) Intermediate
692 alkali-alumino-silicate aqueous solutions released by deeply subducted
693 continental crust; fluid evolution in UHP OH-rich topaz-kyanite quartzites from
694 Donghai (Sulu, China). Journal of Petrology, 48, 1219-1241.
695 Gebauer, D., Schertl, H.-P., Brix, M., and Schreyer, W. (1997) 35 Ma old
696 ultrahigh-pressure metamorphism and evidence for very rapid exhumation in the
697 Dora Maira Massif, Western Alps. Lithos, 41, 5-24.
698 Glodny, J., Ring, U., Kuhn, A., Gleissner, P., and Franz, G. (2005) Crystallization and
699 very rapid exhumation of the youngest Alpine eclogites (Tauern Window,
700 Eastern Alps) from Rb/Sr mineral assemblage analysis. Contributions to

Mineralogy and Petrology, 149, 699-712.

Hacker, B.R., Liou, J.G., Calvert, A., Zhang, R.Y., and Ernst, W.G. (2003) Ultrarapid exhumation of ultrahigh-pressure diamond-bearing metasedimentary rocks of the Kokchetav Massif, Kazakhstan? Lithos, 70, 61-75.

Hacker, B.R., Wallis, S.R., McWilliams, M.O., and Gans, P.B. (2009) $^{40}Ar/^{39}Ar$ Constraints on the tectonic history and architecture of the ultrahigh-pressure Sulu orogen. Journal of Metamorphic Geology, 27, 827-844.

Hawthorne, F.C., and Harlow, G.E. (2008) The crystal chemistry of Al-rich amphiboles: Sadanagaite and potassic-ferrisadanagaite. Canadian Mineralogist, 46, 151-162.

Hawthorne, F.C., Oberti, R., Harlow, G.E., Maresch, W.V., Martin, R.F., Schumacher, J.C., and Welch, M.D. (2012) Nomenclature of the amphibole supergroup. American Mineralogist, 97, 2031-2048.

Hirajima, T., Ishiwatari, A., Cong, B., Zhang, R., Banno, S., and Nozaka, T. (1990) Coesite from Mengzhong eclogite at Donghai country, northeastern Jiangsu province, China. Mineralogical Magazine, 54, 579-583.

Holland, T.J.B. (1989) Dependence of entropy on volume for silicate and oxide minerals; a review and predictive model. American Mineralogist, 74, 5-13.

Holland, T.J.B., and Blundy, J. (1994) Non-ideal interactions in calcic amphiboles and their bearing on amphibole-plagioclase thermometry. Contributions to Mineralogy and Petrology, 116, 433-447.

Holland, T.J.B., and Powell, R. (1998) An internally consistent thermodynamic data set for phases of petrological interest. Journal of Metamorphic Geology, 16, 309-343.

Hoschek, G. (1995) Stability relations and Al content of tremolite and talc in CMASH

assemblages with kyanite + zoisite + quartz + H_2O. European Journal of Mineralogy, 7, 353-362.

Katayama, I., Maruyama, S., Parkinson, C.D., Terada, K., and Sano, Y. (2001) Ion micro-probe U-Pb zircon geochronology of peak and retrograde stages of ultrahigh-pressure metamorphic rocks from the Kokchetav Massif, northern Kazakhstan. Earth and Planetary Science Letters, 188, 185-198.

Kato, T. (2005) New accurate Bence-Albee α-factors for oxides and silicates calculated from the PAP correction procedure. Geostandrds and Geoanalytical Research, 29, 83-94.

Li, X.F., Rusk, B., Wang, R.C., Morishita, Y., Watanabe, Y., and Chen, Z.Y. (2011) Rutile inclusions in quartz crystals record decreasing temperature and pressure during the exhumation of the Su-Lu UHP metamorphic belt in Donghai, East China. American Mineralogist, 96, 964-973.

Li, Z.Y., Li, Y.L., Wijbrans, J.R., Yang, Q.J., Qiu, H.N., and Brouwer, F.M. (2018) Metamorphic P-T Path differences between the two UHP terranes of Sulu Orogen, Eastern China: Petrologic comparison between eclogites from Donghai and Rongcheng. Journal of Earth Science, 29, 1151-1166.

Liu, F.L., Xu, Z., Katayama, I., Yang, J., Maruyama, S., and Liou, J.G. (2001) Mineral inclusions in zircons of para- and orthogneiss from pre-pilot drillhole CCSD-PP1, Chinese Continental Scientific Drilling Project. Lithos, 59, 199-215.

Liu, F.L., and Liou, J.G. (2011) Zircon as the best mineral for P-T-time history of UHP metamorphism: A review on mineral inclusions and U-Pb SHRIMP ages of zircons from the Dabie-Sulu UHP rocks. Journal of Asian Earth Sciences, 40, 1-39.

749 Liu, J.B., Liu, W.Y., Ye, K., and Mao, Q. (2009) Chlorine-rich amphibole in Yangkou
750 eclogite, Sulu ultrahigh-pressure metamorphic terrane, China. European Journal
751 of Mineralogy, 21, 1265-1285.
752 Locock, A.J. (2014) An Excel spreadsheet to classify chemical analyses of amphiboles
753 following the IMA 2012 recommendations. Computers & Geosciences, 62,
754 1–11.
755 Martin, R.F. (2007) Amphiboles in the igneous environment. Reviews in Mineralogy
756 and Geochemistry, 67, 323–358.
757 Massonne, H.J. (2012) Formation of amphibole and clinozoisite-epidote in eclogite
758 owing to fluid Infiltration during exhumation in a subduction channel. Journal of
759 Petrology, 53, 1969-1998.
760 Messiga, B., Tribuzio, R., and Caucia, F. (1991) Amphibole evolution in Variscan
761 eclogite-amphibolites from the Savona crystalline massif (Western Ligurian
762 Alps, Italy); controls on the decompressional P-T-t path. Lithos, 27, 215-230.
763 Medaris Jr, L.G., Brueckner, H.K., Cai, Y., Griffin, W.L., and Janák, M. (2018)
764 Eclogites in peridotite massifs in the Western Gneiss Region, Scandinavian
765 Caledonides: Petrogenesis and comparison with those in the Variscan
766 Moldanubian Zone. Lithos, 322, 325–346.
767 Mogessie, A., Purtscheller, F., and Tessadri, R. (1986) High alumina calcic amphiboles
768 (alumino pargasite-magnesio sadanagaite) from metabasites and metacarbonates
769 of Central Oetztal, Eastern Alps (Northern Tyrol, Austria). Neues Jahrbuch für
770 Mineralogie-Abhandlungen, 154, 21-39.
771 Molina, J.F., Moreno, J.A., Castro, A., Rodriguez, C., and Fershtater, G.B. (2015)
772 Calcic amphibole thermobarometry in metamorphic and igneous rocks: New

calibrations based on plagioclase/amphibole Al-Si partitioning and amphibole/liquid Mg partitioning. Lithos, 232, 286-305.

Nagasaki, A., and Enami, M. (1998) Sr-bearing zoisite and epidote in ultra high-pressure (UHP) metamorphic rocks from the Su-Lu province, eastern China: an important Sr-reservoir under UHP conditions. American Mineralogist, 83, 240-247.

Nishiyama, T., Yoshida-Shiosaki, C., Mori, Y., and Shigeno, M. (2017) Interplay of irreversible reactions and deformation: a case of hydrofracturing in the rodingite-serpentinite system. Progress in Earth and Planetary Science, 4, 1.

O'Brien, P.J. (2019) Tso Morari coesite eclogite: pseudosection predictions v. the preserved record and implications for tectonometamorphic models. In Zhang, L., Zhang, Z., Schertl, H.P., and Wei, C., Eds. HP-UHP Metamorphism and Tectonic Evolution of Orogenic Belts, 474, p. 5-24.

Palin, R.M., St-Onge, M.R., Waters, D.J., Searle, M.P., and Dyck, B. (2014) Phase equilibria modelling of retrograde amphibole and clinozoisite in mafic eclogite from the Tso Morari massif, northwest India: constraining the P-T-M(H_2O) conditions of exhumation. Journal of Metamorphic Geology, 32, 675-693.

Poli, S. (1991) Reaction spaces and p-t paths: from amphibole eclogite to greenschist facies in the Austroalpine domain (Oetztal Complex). Contributions to Mineralogy and Petrology, 106, 399-416.

Powell, R., and Holland, T.J.B. (1988) An internally consistent dataset with uncertainties and correlations: 3. Applications to geobarometry, worked examples and a computer program. Journal of Metamorphic Geology, 6, 173-204.

797 Putnis, A., and Austrheim, H. (2010) Fluid-induced processes: metasomatism and
798 metamorphism. Geofluids, 10, 254-269.
799 Rubatto, D., and Hermann, J. (2001) Exhumation as fast as subduction? Geology, 29,
800 3-6.
801 Savel'eva, V.B., and Korikovskii, S.P. (1998) A sadanagaite in the
802 biotite-corundum-margarite-spinel-anorthite crystalline schists from the West
803 Pribaikal'e. Doklady Earth Sciences, 360, 477–479.
804 Sawaki, T. (1989) Sadanagaite and subsilicic ferroan pargasite from thermally
805 metamorphosed rocks in the Nogo-Hakusan area, central Japan. Mineralogical
806 Magazine, 53, 9-106.
807 Schumacher, J.C. (2007) Metamorphic amphiboles: Composition and coexistence
808 Reviews in Mineralogy and Geochemistry, 67, 359-416.
809 Shimazaki, H., Bunno, M., and Ozawa, T. (1984) Sadanagaite and
810 magnesio-sadanagaite, new silica-poor members of calcic amphibole from
811 Japan. American Mineralogist, 69, 465-471.
812 Shiraishi, K., Oba, T., Suzuki, M., and Ishikawa, K. (1994) Subsilicic magnesian
813 potassium-hastingsite from the Prince Olav Coast, East Antarctica.
814 Mineralogical Magazine, 58, 621-627.
815 Suwa, K., Enami, M., and Horiuchi, T. (1987) Chlorine-rich potassium hastingsite from
816 West Ongul island, Lützow-Holm bay, east Antarctica. Mineralogical Magazine,
817 51, 709-714.
818 Taguchi, T., Miyake, A., Enami, M., and Igami, Y. (2018) Significance of an
819 amorphous SiO_2 phase in a pseudomorph after coesite enclosed in garnet from
820 ultrahigh-pressure eclogite, Su-Lu Belt, eastern China. Journal of Metamorphic

Geology, 36, 843‐854.

Whitney, D.L., and Evans, B.W. (2010) Abbreviations for names of rock–forming minerals. American Mineralogist, 95, 185-187.

Yamasaki, S., Nakamura, D., and Hirajima, T. (2018) Amphibole in UHP eclogite from the Sulu region, eastern China. Journal of Mineralogical and Petrological Sciences, 113, 135–151.

Yang, T.N. (2004) Retrograded textures and associated mass transfer; evidence for aqueous fluid action during exhumation of the Qinglongshan eclogite, southern Sulu ultrahigh pressure metamorphic terrane, eastern China. Journal of Metamorphic Geology, 22, 653-669.

Zhang, R.Y., Hirajima, T., Banno, S., Cong, B.L., and Liou, J.G. (1995) Petrology of ultrahigh-pressure rocks from the southern Su-Lu region, Eastern China. Journal of Metamorphic Geology, 13, 659-675.

Zhang, R.Y., Liou, J.G., and Zheng, J.P. (2004) Ultrahigh-pressure corundum-rich garnetite in garnet peridotite, Sulu terrane, China. Contributions to Mineralogy and Petrology, 147, 21-31.

Zhang, R.Y., Liou, J.G., and Ernst, W.G. (2009) The Dabie-Sulu continental collision zone; a comprehensive review. Gondwana Research, 16, 1-26.

Zhang, Z.M., Xu, Z.Q., and Xu, H.F. (2000) Petrology of ultrahigh-pressure eclogites from the ZK703 drillhole in the Donghai, eastern China. Lithos, 52, 35-50.

Zhang, Z.M., Xiao, Y., Liu, F., Liou, J.G., and Hoefs, J. (2005) Petrogenesis of UHP metamorphic rocks from Qinglongshan, southern Sulu, east-central China. Lithos, 81, 189-207.

Zhang, Z.M., Shen, K., Xiao, Y.L., Hoefs, J., and Liou, J.G. (2006) Mineral and fluid

inclusions in zircon of UHP metamorphic rocks from the CCSD-main drill hole; a record of metamorphism and fluid activity. Lithos, 92, 378-398.

Zhang, Z.M., Shen, K., Sun, W., Liu, Y., Liou, J.G., Shi, C., and Wang, J. (2008) Fluids in deeply subducted continental crust; petrology, mineral chemistry and fluid inclusion of UHP metamorphic veins from the Sulu Orogen, eastern China. Geochimica et Cosmochimica Acta, 72, 3200-3228.

Zhang, Z.M., Dong, X., Liou, J.G., Liu, F., Wang, W., and Yui, F. (2011) Metasomatism of garnet peridotite from Jiangzhuang, southern Sulu UHP belt: constraints on the interactions between crust and mantle rocks during subduction of continental lithosphere. Journal of Metamorphic Geology, 29, 917-937.

Figure captions

Figure 1. (a) Simplified map of the Sulu region showing major tectonic units and the position of the Donghai area (slightly modified Fig. 1 from Zhang et al., 2008). (b) Schematic geological map showing the distribution of eclogites in the Donghai area and sample localities (slightly modified Fig. 2 from Zhang et al., 1995). Abbreviations: WQY fault, Wulian–Qingdao-Yantai fault; JX fault, Jiashan-Xiangshui fault.

Figure 2. (a), (b), and (d) Polarizing microscope photographs (plane polarized light) and (c) back-scattered electron (BSE) image of quartz-bearing eclogites from the Donghai area, Sulu UHP metamorphic belt. CaKα X-ray and electron back-scattered diffraction (EBSD) pattern maps of the area of (d) are shown in Fig. 6a and 9, respectively. Abbreviations: Symp, symplectite after omphacite.

Figure 3. Compositional ranges of amphibole in eclogites of (a) JDQ03, (b) 91CHXX, and (c) 91CH08 from the Donghai area, Sulu UHP metamorphic belt, on the ^{C}(Al + Fe^{3+} + Cr + 2Ti)–^{A}(Na +K) and Si–^{B}Na diagrams. * Some ferro-sadanagaite and ferro-taramite grains belong to potassic category with K > Na in the A site.

Figure 4. (a) Back-scattered electron (BSE) image showing textural relationship of garnet porphyroblast, Amp (O), and Amp (S) in an eclogite (JDQ03) from the Donghai area, Sulu UHP metamorphic belt. (b) Step-scan analysis of the amphibole around garnet along the line A-A' in Fig. 4a, and comparison of its compositional range with those in symplectite and the matrix. Abbreviations are: av, average; max, maximum; med, median: min, minimum. * Outliers are not plotted.

Figure 5. (a) Back-scattered electron (BSE) image showing textural relationship of garnet porphyroblast, Amp (O), and Amp (S) in an eclogite (91CHXX) from the

Donghai area, Sulu UHP metamorphic belt. (b) Step-scan analysis of the amphibole around garnet along the line B-B' in Fig. 5a, and comparison of its compositional range with those in symplectite and the matrix. * Outliers are not plotted.

Figure 6. (a) CaKα X-ray map showing textural relationship of garnet porphyroblast and amphibole [Amp (O), Amp (Q), Amp (G), and Amp (S)] in an eclogite (91CH08) from the Donghai area, Sulu UHP metamorphic belt. Step-scan analyses of the amphibole segments between (b) garnet and symplectite and between (c) garnet and quartz along the lines C-C' and D–D' in Fig. 6a, respectively. Figure 6b compares the compositional range of the Amp (O) segment with those in symplectite [Amp (S)]. (d) Step-scan analysis of crack-filling amphibole segments [Amp (G)] between garnet segments along the line E-E' in Fig. 6a. * Outliers are not plotted.

Figure 7. (a) High-angle annular dark field scanning TEM (HAADF-STEM) image and (b) bright-field (BF)-TEM image of subsilicic amphibole–garnet interface in an eclogite (91CHXX) from the Donghai area, Sulu UHP metamorphic belt. Bright-field TEM image of the interface structures was viewed along the [001] zone axis of aluminous amphibole.

Figure 8. Electron back-scattered diffraction (EBSD) pattern maps of (a) Amp (O) and Amp (S) and (b) symplectitic sodic diopside in an eclogite (91CHXX: 1 μm grid step). Pole figures for crystallographic orientations of (100), (010), and [001] of the (c) Amp (S) and (d) sodic diopside particles in the selective domains 1–4 of symplectite. Data N indicates the number of analysis particles. Circles in (a) indicate direct connection between Amp (O) and Amp (S).

Figure 9. Electron back-scattered diffraction (EBSD) pattern map of Amp (O), Amp (Q), Amp (G), and Amp (S) in an eclogite (91CH08: 2 μm grid step) from the Donghai area, Sulu UHP metamorphic belt.

Figure 10. (a) Electron back-scattered diffraction (EBSD) pattern map (1 μm grid step) of Amp (Q) and Amp (G) in an eclogite (91CH08) from the Donghai area, Sulu UHP metamorphic belt. (b) Equal-area and lower hemisphere projection showing crystallographic orientations of the Amp (Q) and Amp (G) segments. Data n indicates the number of analysis points. (c) Step-scan analysis of the boundary between the Amp (Q) and Amp (G) segments along the line F-F' in Fig. 10a.

Figure 11. (a) Electron back-scattered diffraction (EBSD) pattern map (1 μm grid step) of Amp (O), Amp (G), and Amp (S) in an eclogite (91CH08) from the Donghai area, Sulu UHP metamorphic belt. Equal-area and lower hemisphere projection comparison of crystallographic orientations of the Amp (O) and Amp (S) segments in the sets of (b) domains 8, 9, and 10 and (c) domains 11, 12, and 13. Data n indicates the number of analysis points. Circles in (a) indicate a direct connection between Amp (O) and Amp (S).

Figure 12. Comparison of the estimated equilibrium P-T conditions of aluminous calcium amphiboles + plagioclase (this study) and the exhumation P-T path of Donghai eclogites reported in literature. Abbreviations for references are: C18, Curetti et al. (2018); F07, Frezzotti et al. (2007); L11, Li et al. (2011); L18, Li et al. (2018); Z95, Zhang et al. (1995); Z05, Zhang et al. (2005). Geothermometer (HB94) and geobarometer (M15) are from Holland and Blundy (1994) and Molina et al. (2015), respectively. The univariant lines of Dia-Gr, Coe-Qz, Ab-Jd+Qz, and Al_2SiO_5 phases were calculated using THERMOCALC software

928 ver. 3.33 (Powell and Holland, 1988), internally consistent thermodynamic data
929 set (Holland and Powell, 1998; updated June 2009), and program AX_2
930 (https://filedn.com/lU1GlyFhv3UuXg5E9dbnWFF/TJBHpages/ax.html).
931 Figure 13. Conceptual diagram of growth scenarios (Models 1 and 2) of retrograde
932 amphiboles in the Donghai eclogites, Sulu UHP metamorphic belt during the
933 exhumation and hydration stage. (a) Eclogite facies and early exhumation stage.
934 (b) Formations of sodic diopside + plagioclase symplectite and crack-filling
935 amphibole [Amp (G)] at the early exhumation and hydration stage, although it is
936 not clear which of these phenomena proceeded first, or if they were nearly
937 simultaneous. (c) Formations of mantle amphibole around garnet [Amp (O) and
938 Amp (Q)] and symplectitic amphibole [Amp (S)] (Model 2). (d1) Initial
939 nucleation of amphibole at the interface between garnet and symplectite of sodic
940 diopside + plagioclase, and subsequent growth of Amp (S) and Amp (O)/Amp
941 (Q). The inner and outer zones of Amp (O) and Amp (Q) grew inward and
942 outward from the initial surface of the garnet (dashed line), respectively (Model
943 1). (d2) The formation of the inner and outer zones of Amp (O) and Amp (Q) by
944 modification of the chemical composition of their outer parts due to
945 re-equilibration (Model 2).
946 Figure 14. Volume change of minerals [(a) in cm^3 and (b) %] based on the calculated
947 stoichiometric coefficients of minerals as a function of $a = \xi_6/\xi_5$, where ξ_5 and ξ_6
948 represent the reaction extents of R5 and R6 in the text, respectively. The mineral
949 volumes were estimated using the molar volumes listed in Table 3. The
950 estimated volume proportions (%) of Amp (Q), aegirine-diopside, and
951 plagioclase in the reaction zone are plotted in Fig. 14b for discussion on the

952 possible range of the parameter *a*. (c) Stoichiometric coefficients of mobile

953 components as a function of the parameter *a*.

954

955

This is the peer-reviewed, final accepted version for American Mineralogist, published by the Mineralogical Society of America.
The published version is subject to change. Cite as Authors (Year) Title. American Mineralogist, in press.
DOI: https://doi.org/10.2138/am-2022-7996. http://www.minsocam.org/

Table 1. Representative chemical compositions of retrograde amphibole in SiO_2 phase-bearing eclogites from the Donghai area, Su-Lu UHP metamorphic belt.

Sample	JDQ03					91CHXX					91CH08					
Texture	Inclusior	Matrix	Amp (O)		Amp (S)	Inclusion	Matrix	Amp (O)		Amp (S)	Amp (O)		Amp (Q)		Amp (G)	Amp (S)
Zone			Inner	Outer				Inner	Outer		Inner	Outer	Inner	Outer		
Mineral	Ftrm	Fsdg	Sdg	Prg	Prg	Fsdg	Prg	Fsdg	Prg	Prg	Fsdg	Fsdg	Fsdg	Ftrm	Fsdg	Trm
wt%																
SiO_2	39.29	38.50	37.20	40.15	42.87	38.64	37.82	36.39	40.17	41.00	36.22	37.93	35.70	38.26	36.01	41.82
TiO_2	0.83	0.16	0.03	0.07	0.17	0.15	0.11	0.06	0.13	0.23	0.07	0.07	0.01	0.01	0.08	0.34
Al_2O_3	17.32	19.77	20.35	15.73	12.84	18.77	17.10	20.40	14.96	14.15	20.16	16.28	19.89	17.26	20.14	18.79
Cr_2O_3	0.00	0.15	0.01	0.00	0.03	0.00	0.00	0.01	0.03	0.05	0.01	0.01	0.00	0.00	0.02	0.00
FeO[a]	18.32	19.01	16.26	14.34	12.83	17.81	16.98	17.35	16.79	17.12	21.30	21.12	21.91	22.16	21.48	12.77
MnO	0.12	0.23	0.21	0.19	0.13	0.16	0.19	0.17	0.18	0.19	0.44	0.36	0.45	0.39	0.46	0.24
MgO	6.63	5.37	7.41	10.69	12.65	7.09	8.74	7.23	9.42	10.12	3.97	5.88	3.79	4.33	4.33	9.74
CaO	8.94	9.26	10.42	10.82	10.95	9.19	11.73	11.19	11.34	11.60	9.47	9.07	9.36	8.36	9.60	7.63
Na_2O	4.73	3.95	3.64	3.24	3.29	4.49	3.57	3.32	3.18	3.19	3.64	3.63	3.46	3.53	4.36	6.02
K_2O	0.67	1.08	0.78	1.17	0.88	0.08	0.05	0.06	0.11	0.08	1.69	2.04	1.98	2.32	0.33	0.43
F	b.d.	b.d.	b.d.	b.d.	b.d.	b.d.	b.d.	b.d.	b.d.	b.d.	b.d.	b.d.	b.d.	b.d.	b.d.	b.d.
Cl	1.32	1.60	0.02	0.04	0.04	b.d.	b.d.	b.d.	b.d.	b.d.	b.d.	b.d.	b.d.	b.d.	b.d.	b.d.
O=F, Cl	-0.30	-0.36	0.00	-0.01	-0.01											
Total	97.87	98.72	96.33	96.43	96.67	96.38	96.29	96.18	96.31	97.73	96.97	96.39	96.55	96.62	96.81	97.78
Formulae [24 (OH, F, Cl, O)]																
Si	5.969	5.836	5.638	6.030	6.374	5.845	5.758	5.552	6.095	6.126	5.597	5.876	5.558	5.944	5.541	6.074
Ti	0.095	0.018	0.003	0.008	0.019	0.017	0.013	0.007	0.015	0.026	0.008	0.008	0.001	0.001	0.009	0.037
Al	3.101	3.532	3.635	2.784	2.251	3.346	3.069	3.669	2.675	2.492	3.672	2.973	3.650	3.160	3.653	3.216
Cr	0.000	0.018	0.001	0.000	0.004	0.000	0.000	0.001	0.004	0.006	0.001	0.002	0.000	0.000	0.002	0.000
Fe^{3+b}	0.508	0.287	0.405	0.424	0.267	0.492	0.503	0.354	0.341	0.464	0.565	0.768	0.673	0.569	0.685	0.452
Fe^{2+b}	1.820	2.123	1.656	1.378	1.329	1.761	1.659	1.859	1.789	1.676	2.188	1.969	2.180	2.310	2.079	1.099
Mn	0.016	0.030	0.027	0.024	0.016	0.020	0.024	0.022	0.023	0.024	0.058	0.047	0.059	0.051	0.060	0.030
Mg	1.502	1.213	1.674	2.393	2.804	1.599	1.984	1.645	2.131	2.254	0.915	1.358	0.880	1.003	0.993	2.109
Ca	1.455	1.504	1.692	1.741	1.745	1.489	1.914	1.829	1.844	1.857	1.568	1.506	1.561	1.392	1.583	1.187
Na	1.393	1.161	1.070	0.944	0.948	1.317	1.054	0.982	0.935	0.924	1.090	1.090	1.044	1.063	1.301	1.696
K	0.130	0.209	0.151	0.224	0.167	0.015	0.010	0.012	0.021	0.015	0.333	0.403	0.393	0.460	0.065	0.080
Total	15.989	15.931	15.952	15.950	15.924	15.901	15.988	15.932	15.873	15.864	15.995	16.000	15.999	15.953	15.971	15.980
X_{Mg}	0.452	0.364	0.503	0.635	0.678	0.476	0.545	0.469	0.544	0.574	0.295	0.408	0.288	0.303	0.323	0.657

[a] Total iron as FeO.

[b] Calculated value (see text)

Abbreviations: Amp (O), amphibole segment between garnet and symplectite; Amp (S), amphibole in symplectite after omphacite; Amp (Q), amphibole segment between garnet and matrix quartz; Amp (G), crack-filling amphibole; b.d., below the detection limit.

Table 2. Pressure-temperature conditions of amphibole-plagioclase sets estimated using amphibole-plagioclase geothermobarometers.

Sample	JDQ03 (An_{10})[a]		91CHXX (An_{16})		91CH08 (An_{11})	
	T (°C)[b]	P (GPa)[c]	T (°C)	P (GPa)	T (°C)	P (GPa)
Amp (O)	675 (4)[d]	0.97 (4)	686 (10)	0.92 (2)	696 (33)	1.28 (18)
Amp (Q)					694 (14)	1.32 (14)
Amp (S)	674(16)	0.86 (6)	701 (6)	0.83 (2)	729 (22)	1.33 (20)

[a] Average anorthite content employed for the calculations.

[b] Amp-Pl geothermometer B of Holland and Blundy (1994).

[c] Pl-Amp Al/Si partitioning geobarometer of Molina et al. (2015).

[d] Number in parentheses indicates standard deviation (1σ level), which corresponds to the last digit of the average value, estimated based on the calculations using several data sets of amphibole-plagioclase compositions.

Abbreviations: Amp (O), amphibole segment between garnet and symplectite; Amp (Q), amphibole segment between garnet and matrix quartz; Amp (S), amphibole in symplectite after omphacite.

Table 3. Chemical compositions and molar volumes of Amp (Q) and related minerals for the SVD analysis.

	Si[a]	Al[a]	Fe[b]	Mn	Mg	Ca[a]	Na	K	Total	Volume (cm^3/mol)[c]
Reactants										
Grt	3.00	1.96	1.52	0.05	0.40	1.07	0.00	0.00	8.00	118.5
Qz	1.00	0.00	0.00	0.00	0.00	0.00	0.00	0.00	1.00	22.7
Products										
Amp (Q)	5.61	3.59	2.86	0.06	0.88	1.54	1.04	0.40	15.98	277.4
Aeg-di	2.00	0.06	0.75	0.02	0.17	0.42	0.58	0.00	4.00	65.5
Pl	2.89	1.11	0.00	0.00	0.00	0.11	0.89	0.00	5.00	100.1

[a] Matrix of mineral compositions used for the SVD analysis.

[b] $Fe^{2+} + Fe^{3+}$.

[c] Calculated using end-member data of Holland (1989) and Holland and Powell (1998).

This is the peer-reviewed, final accepted version for American Mineralogist, published by the Mineralogical Society of America.
The published version is subject to change. Cite as Authors (Year) Title. American Mineralogist, in press.
DOI: https://doi.org/10.2138/am-2022-7996. http://www.minsocam.org/

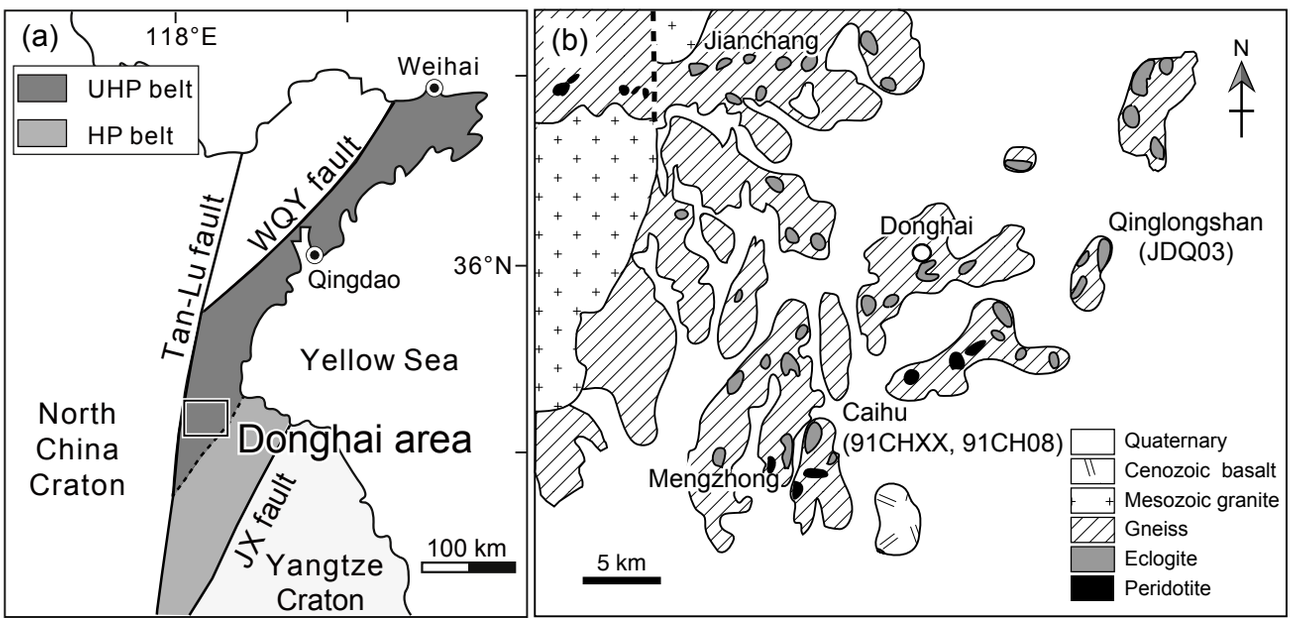

Figure 1. (a) Simplified map of the Sulu region showing major tectonic units and the position of the Donghai area (slightly modified Fig. 1 from Zhang et al., 2008) . (b) Schematic geological map showing the distribution of eclogites in the Donghai area and sample localities (slightly modified Fig. 2 from Zhang et al., 1995). Abbreviations: WQY fault, Wulian–Qingdao-Yantai fault; JX fault, Jiashan-Xiangshui fault.

Fig. 1 (Enami and others)

This is the peer-reviewed, final accepted version for American Mineralogist, published by the Mineralogical Society of America.
The published version is subject to change. Cite as Authors (Year) Title. American Mineralogist, in press.
DOI: https://doi.org/10.2138/am-2022-7996. http://www.minsocam.org/

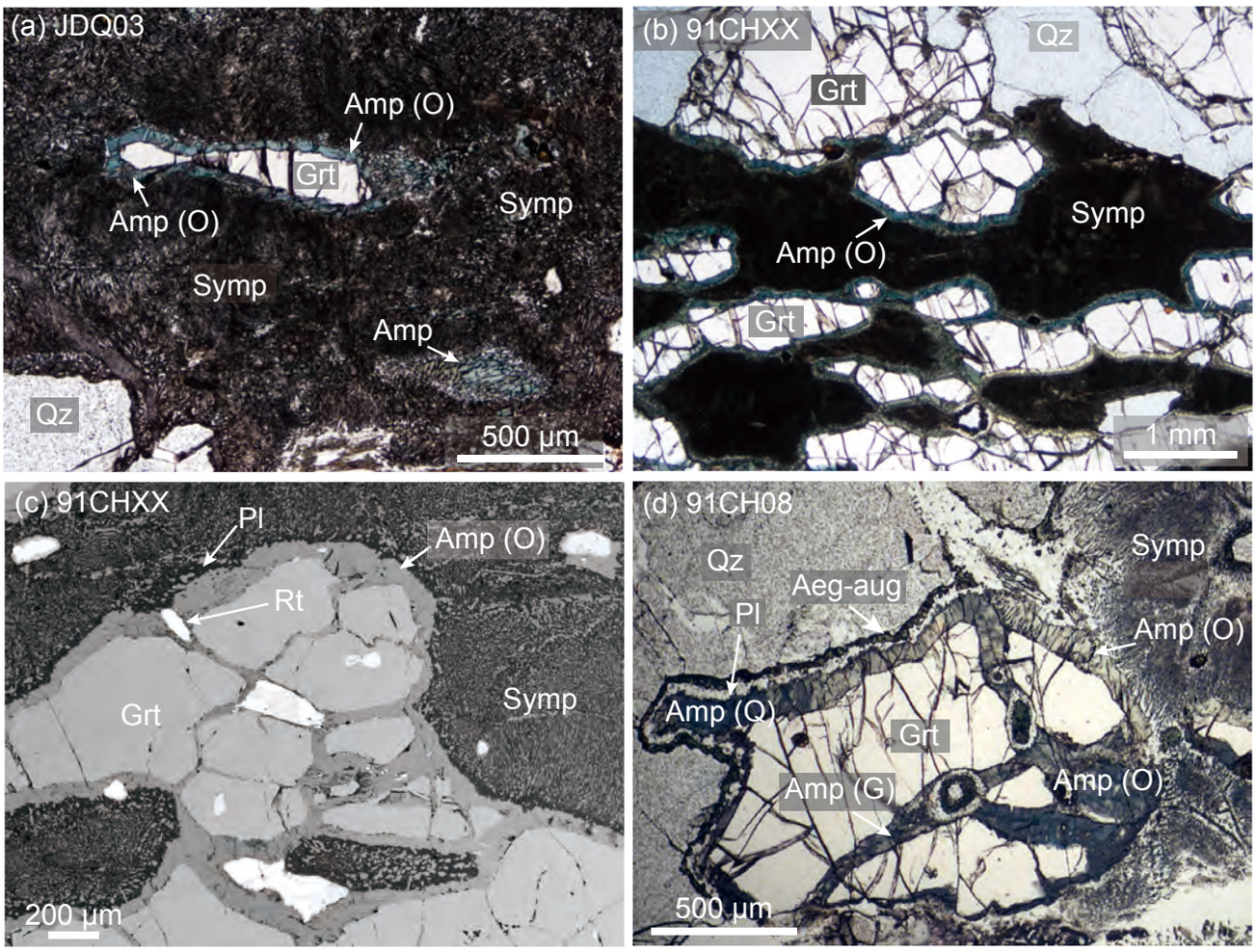

Figure 2. (a), (b), and (d) Polarizing microscope photographs (plane polarized light) and (c) back-scattered electron (BSE) image of quartz-bearing eclogites from the Donghai area, Sulu UHP metamorphic belt. CaKα X-ray map and electron back-scattered diffraction (EBSD) pattern map of the area of (d) are shown in Fig. 6a and 9, respectively. Abbreviations: Symp, symplectite after omphacite.

Fig. 2 (Enami and others)

This is the peer-reviewed, final accepted version for American Mineralogist, published by the Mineralogical Society of America.
The published version is subject to change. Cite as Authors (Year) Title. American Mineralogist, in press.
DOI: https://doi.org/10.2138/am-2022-7996. http://www.minsocam.org/

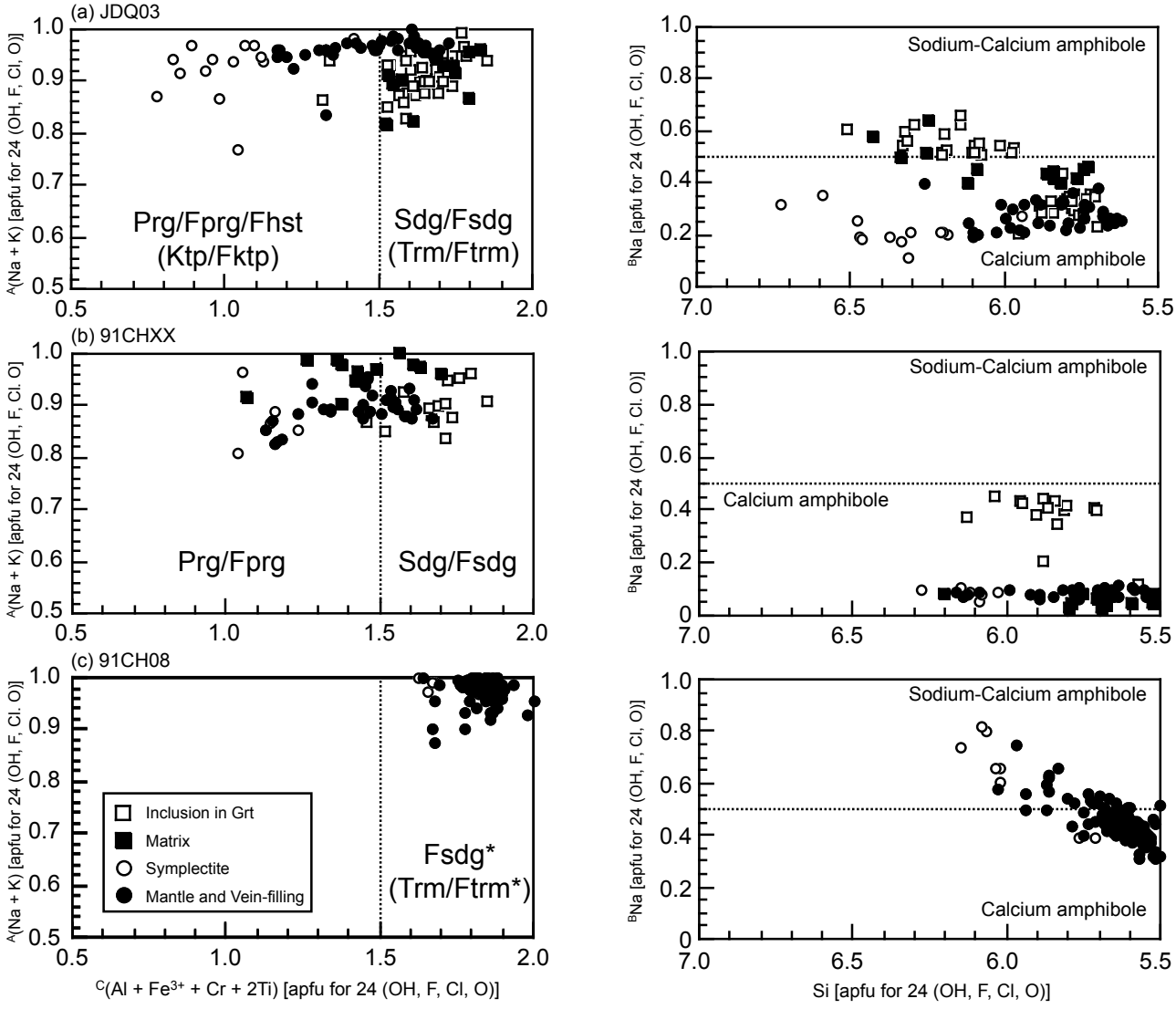

Figure 3. Compositional ranges of amphibole in eclogites of (a) JDQ03, (b) 91CHXX, and (c) 91CH08 from the Donghai area, Sulu UHP metamorphic belt, on the $^{[C]}(Al + Fe^{3+} + Cr + 2Ti)$-$^{[A]}(Na + K)$ and Si-$^{[B]}Na$ diagrams.

* Some ferro-sadanagaite and ferro-taramite grains belong to potassic category with K > Na in the [A] site.

Fig. 3 (Enami and others)

This is the peer-reviewed, final accepted version for American Mineralogist, published by the Mineralogical Society of America.
The published version is subject to change. Cite as Authors (Year) Title. American Mineralogist, in press.
DOI: https://doi.org/10.2138/am-2022-7996. http://www.minsocam.org/

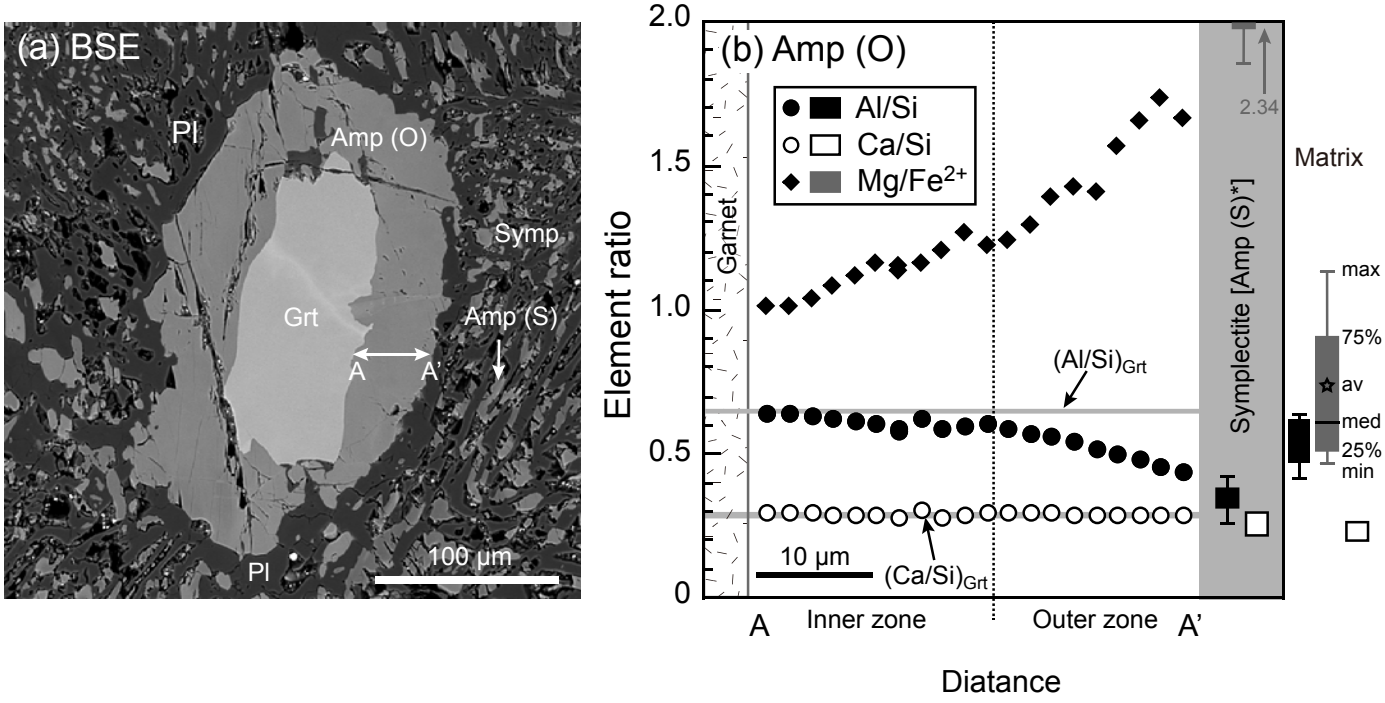

Figure 4. (a) Back-scattered electron (BSE) image showing textural relationship of garnet porphyroblast, Amp (O), and Amp (S) in an eclogite (JDQ03) from the Donghai area, Sulu UHP metamorphic belt. (b) Step-scan analysis of the amphibole around garnet along the line A-A' in Fig. 4a, and comparison of its compositional range with those in symplectite and the matrix. Abbreviations are: av, average; max, maximum; med, median: min, minimum.
* Outliers are not plotted.

Fig. 4 (Enami and others)

This is the peer-reviewed, final accepted version for American Mineralogist, published by the Mineralogical Society of America.
The published version is subject to change. Cite as Authors (Year) Title. American Mineralogist, in press.
DOI: https://doi.org/10.2138/am-2022-7996. http://www.minsocam.org/

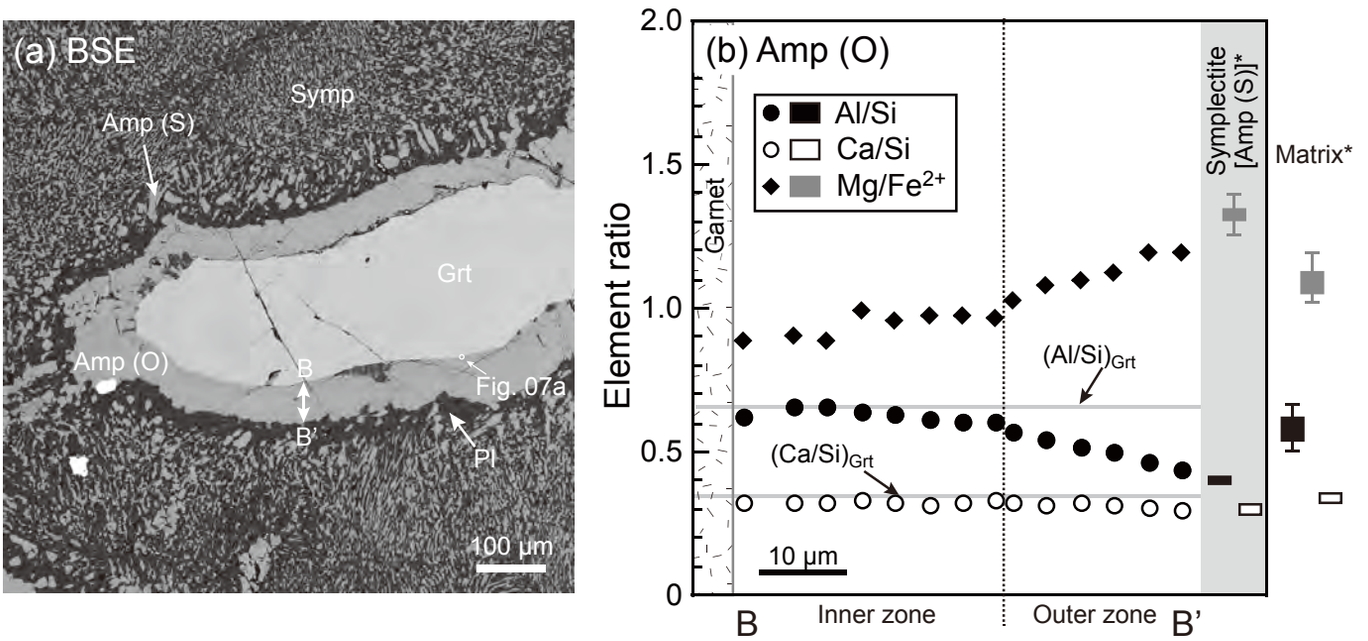

Figure 5. (a) Back-scattered electron (BSE) image showing textural relationship of garnet porphyroblast, Amp (O), and Amp (S) in an eclogite (91CHXX) from the Donghai area, Sulu UHP metamorphic belt. (b) Step-scan analysis of the amphibole around garnet along the line B-B' in Fig. 5a, and comparison of its compositional range with those in symplectite and the matrix. * Outliers are not plotted.

Fig. 5 (Enami and others)

This is the peer-reviewed, final accepted version for American Mineralogist, published by the Mineralogical Society of America.
The published version is subject to change. Cite as Authors (Year) Title. American Mineralogist, in press.
DOI: https://doi.org/10.2138/am-2022-7996. http://www.minsocam.org/

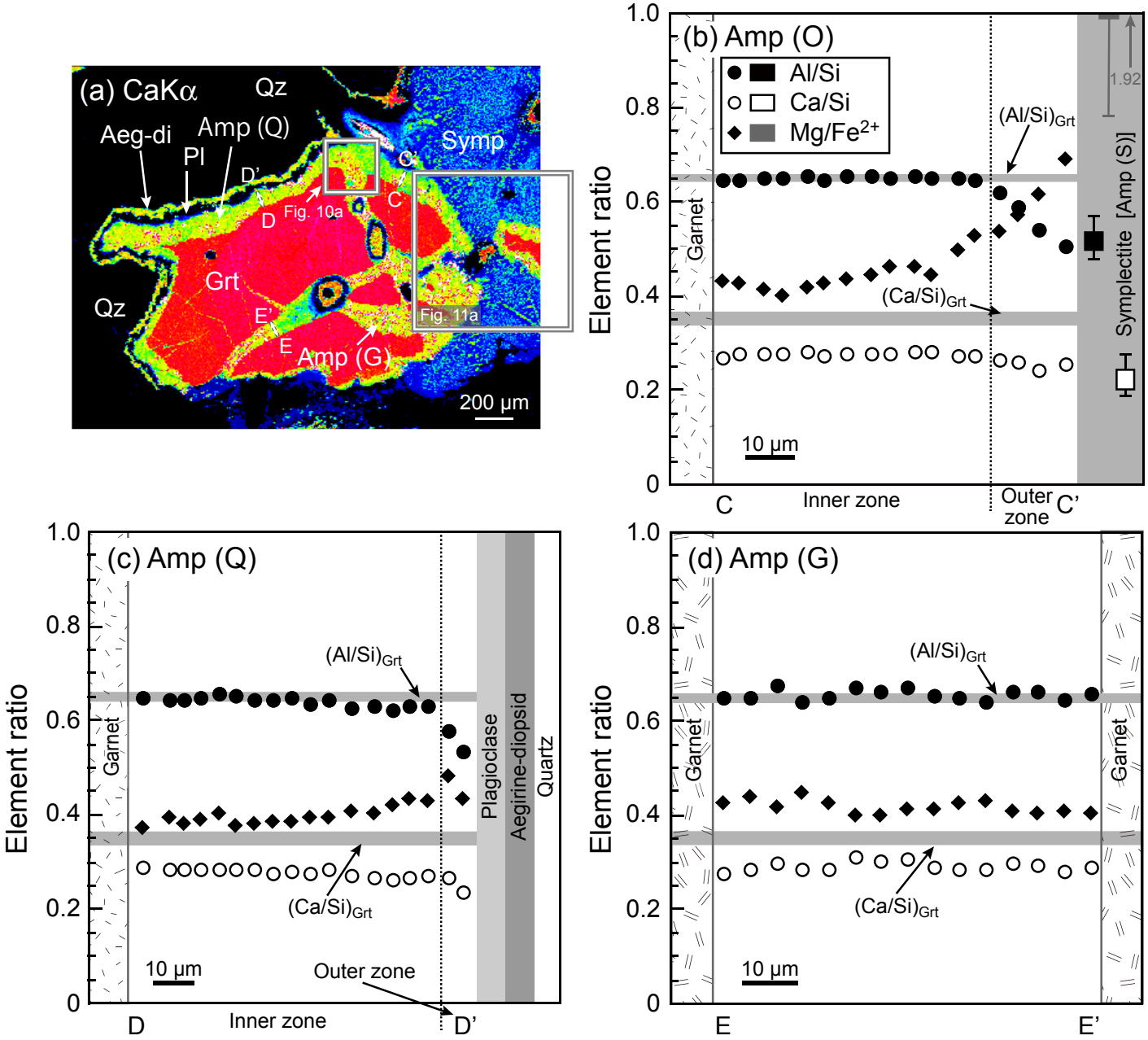

Figure 6. (a) CaKα X-ray map showing textural relationship of garnet porphyroblast and amphibole [Amp (O), Amp (Q), Amp (G), and Amp (S)] in an eclogite (91CH08) from the Donghai area, Sulu UHP metamorphic belt. Step-scan analyses of the amphibole segments between (b) garnet and symplectite and between (c) garnet and quartz along the lines C-C' and D–D' in Fig. 6a, respectively. Figure 6b compares the compositional range of the Amp (O) segment with those in symplectite [Amp (S)]. (d) Step-scan analysis of crack-filling amphibole segments [Amp (G)] between garnet segments along the line E-E' in Fig. 6a.

Fig. 6 (Enami and others)

This is the peer-reviewed, final accepted version for American Mineralogist, published by the Mineralogical Society of America.
The published version is subject to change. Cite as Authors (Year) Title. American Mineralogist, in press.
DOI: https://doi.org/10.2138/am-2022-7996. http://www.minsocam.org/

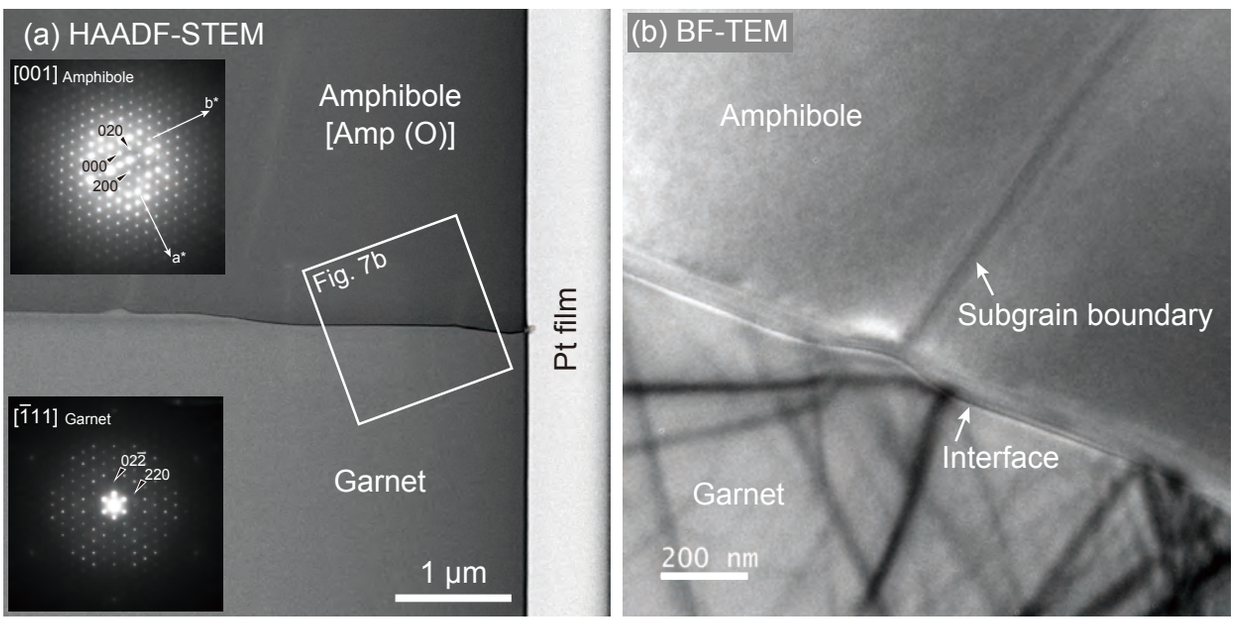

Figure 7. (a) High-angle annular dark field scanning TEM (HAADF-STEM) image and (b) bright-field (BF)-TEM image of aluminous amphibole–garnet interface in an eclogite (91CHXX) from the Donghai area, Sulu UHP metamorphic belt. Bright-field TEM image of the interface structures was viewed along the [001] zone axis of aluminous amphibole.

Fig. 7 (Enami and others)

This is the peer-reviewed, final accepted version for American Mineralogist, published by the Mineralogical Society of America.
The published version is subject to change. Cite as Authors (Year) Title. American Mineralogist, in press.
DOI: https://doi.org/10.2138/am-2022-7996. http://www.minsocam.org/

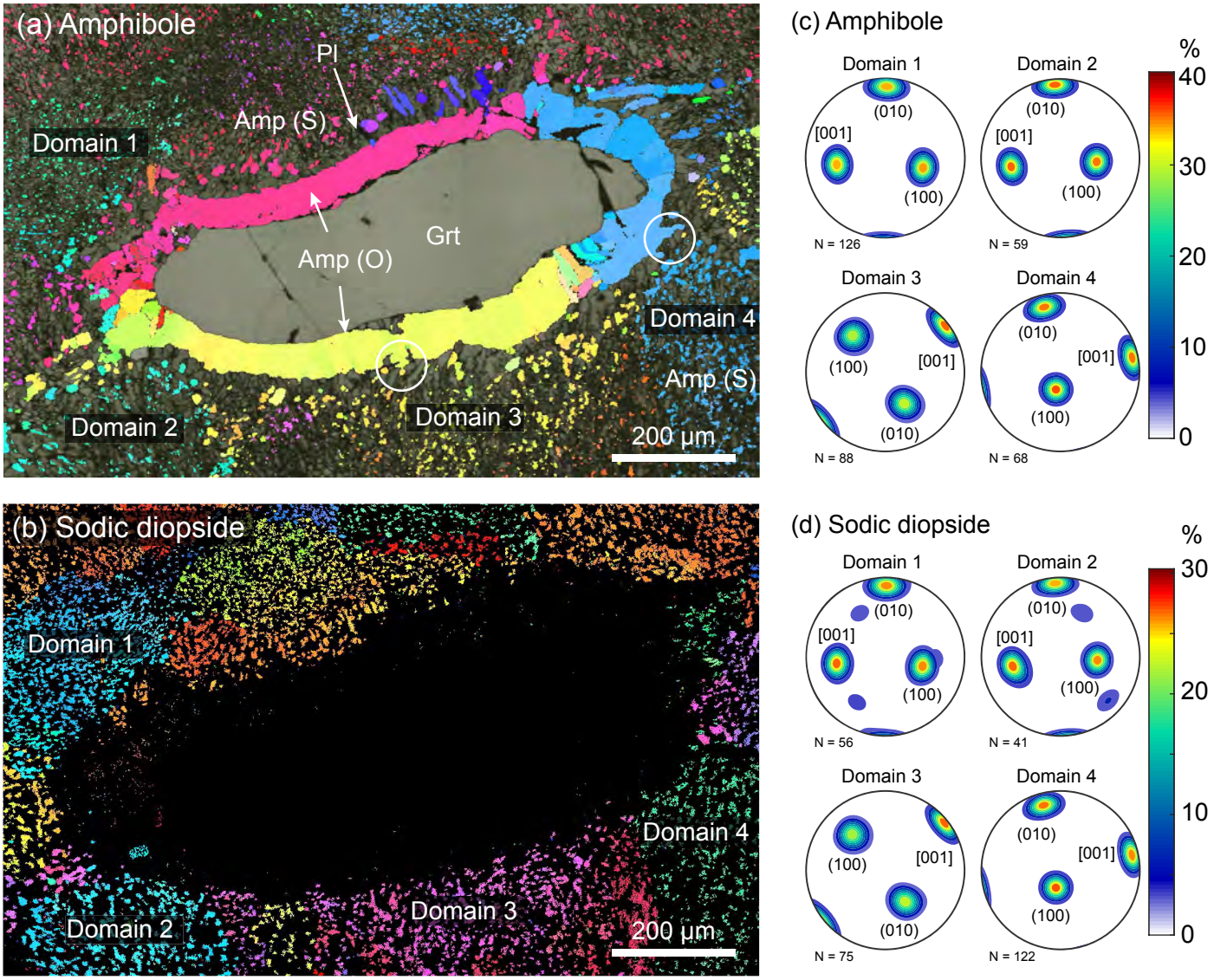

Figure 8. Electron back-scattered diffraction (EBSD) pattern maps of (a) Amp (O) and Amp (S) and (b) symplectitic sodic diopside in an eclogite (91CHXX: 1 μm grid step). Pole figures for crystallographic orientations of (100), (010), and [001] of the (c) Amp (S) and (d) sodic diopside particles in the selective domains 1–4 of symplectite. Data N indicates the number of analysis particles. Circles in (a) indicate a direct connection between Amp (O) and Amp (S).

Fig. 8 (Enami and others)

This is the peer-reviewed, final accepted version for American Mineralogist, published by the Mineralogical Society of America.
The published version is subject to change. Cite as Authors (Year) Title. American Mineralogist, in press.
DOI: https://doi.org/10.2138/am-2022-7996. http://www.minsocam.org/

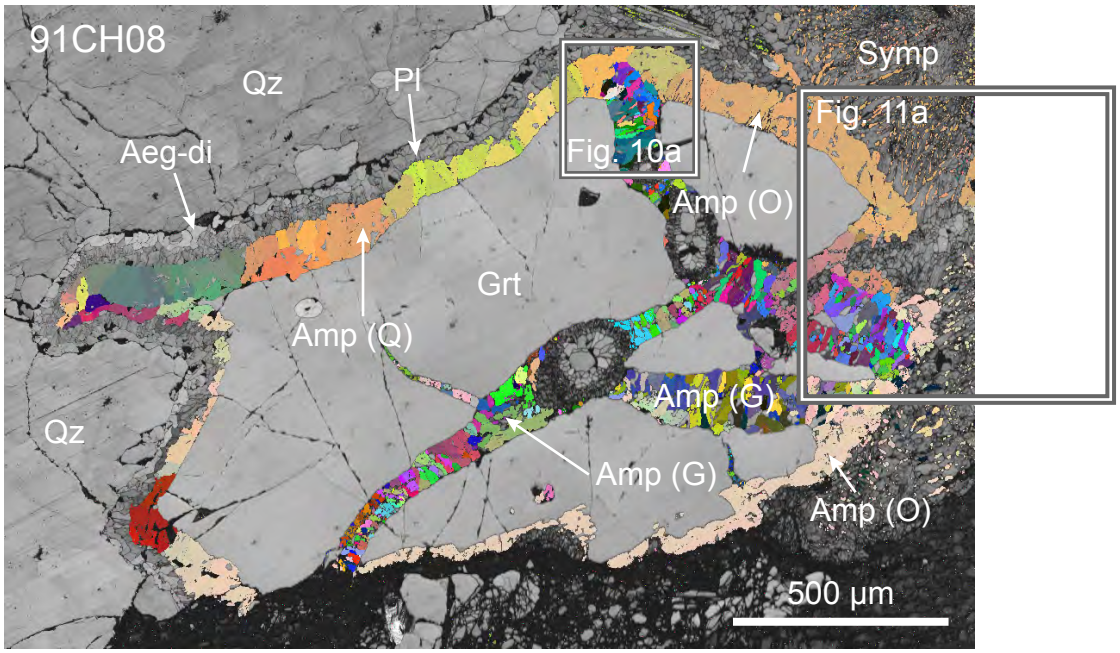

Figure 9. Electron back-scattered diffraction (EBSD) pattern map of Amp (O), Amp (Q), Amp (G), and Amp (S) in an eclogite (91CH08: 2 μm grid step) from the Donghai area, Sulu UHP metamorphic belt.

Fig. 9 (Enami and others)

This is the peer-reviewed, final accepted version for American Mineralogist, published by the Mineralogical Society of America.
The published version is subject to change. Cite as Authors (Year) Title. American Mineralogist, in press.
DOI: https://doi.org/10.2138/am-2022-7996. http://www.minsocam.org/

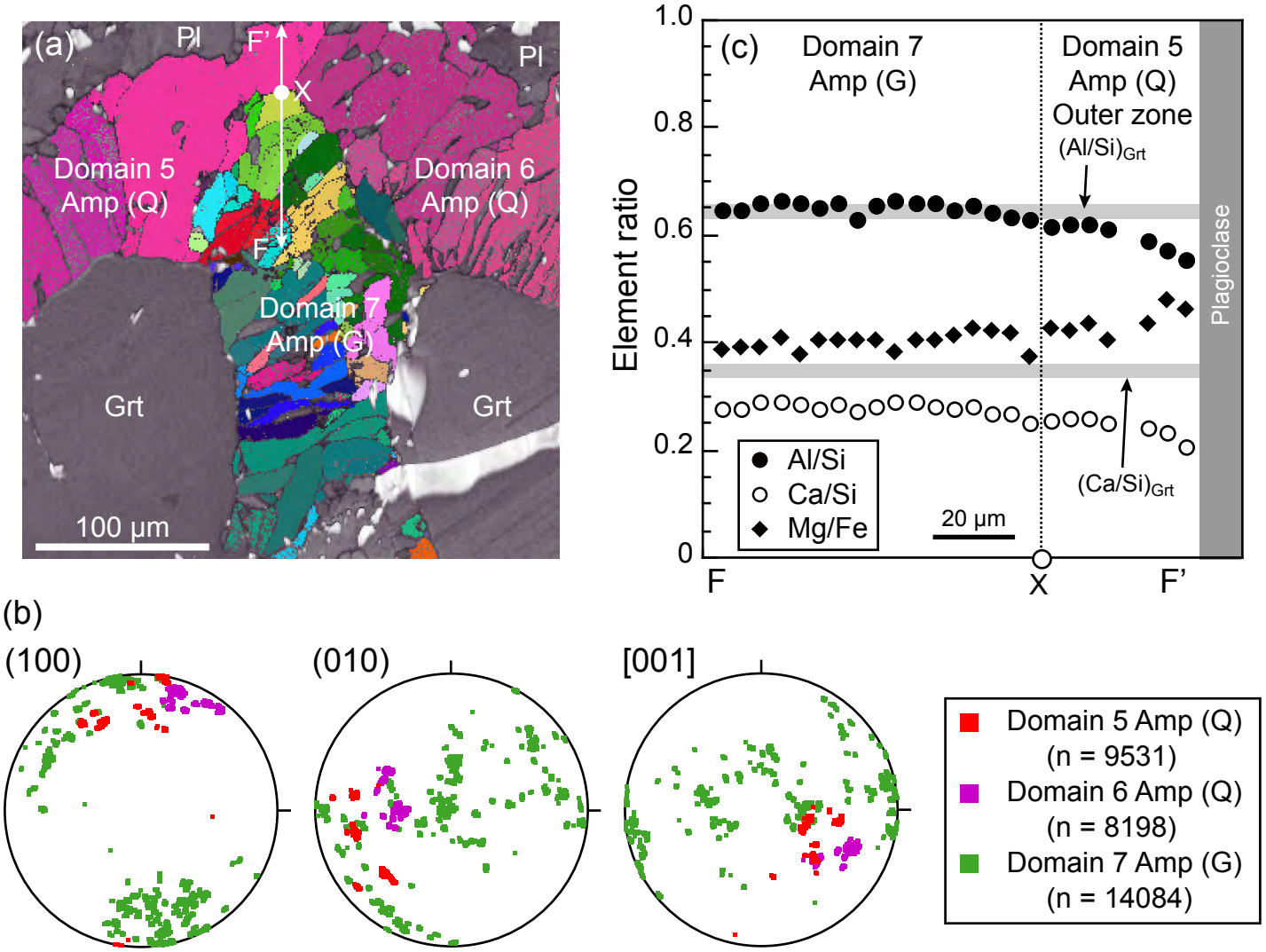

Figure 10. (a) Electron back-scattered diffraction n (EBSD) pattern map (1 μm grid step) of Amp (Q) and Amp (G) in an eclogite (91CH08) from the Donghai area, Sulu UHP metamorphic belt. (b) Equal-area and lower hemisphere projection showing crystallographic orientations of the Amp (Q) and Amp (G) segments. Data n indicates the number of analysis points. (c) Step-scan analysis of the boundary between the Amp (Q) and Amp (G) segments along the line F-F' in Fig. 10a.

Fig. 10 (Enami and others)

This is the peer-reviewed, final accepted version for American Mineralogist, published by the Mineralogical Society of America.
The published version is subject to change. Cite as Authors (Year) Title. American Mineralogist, in press.
DOI: https://doi.org/10.2138/am-2022-7996. http://www.minsocam.org/

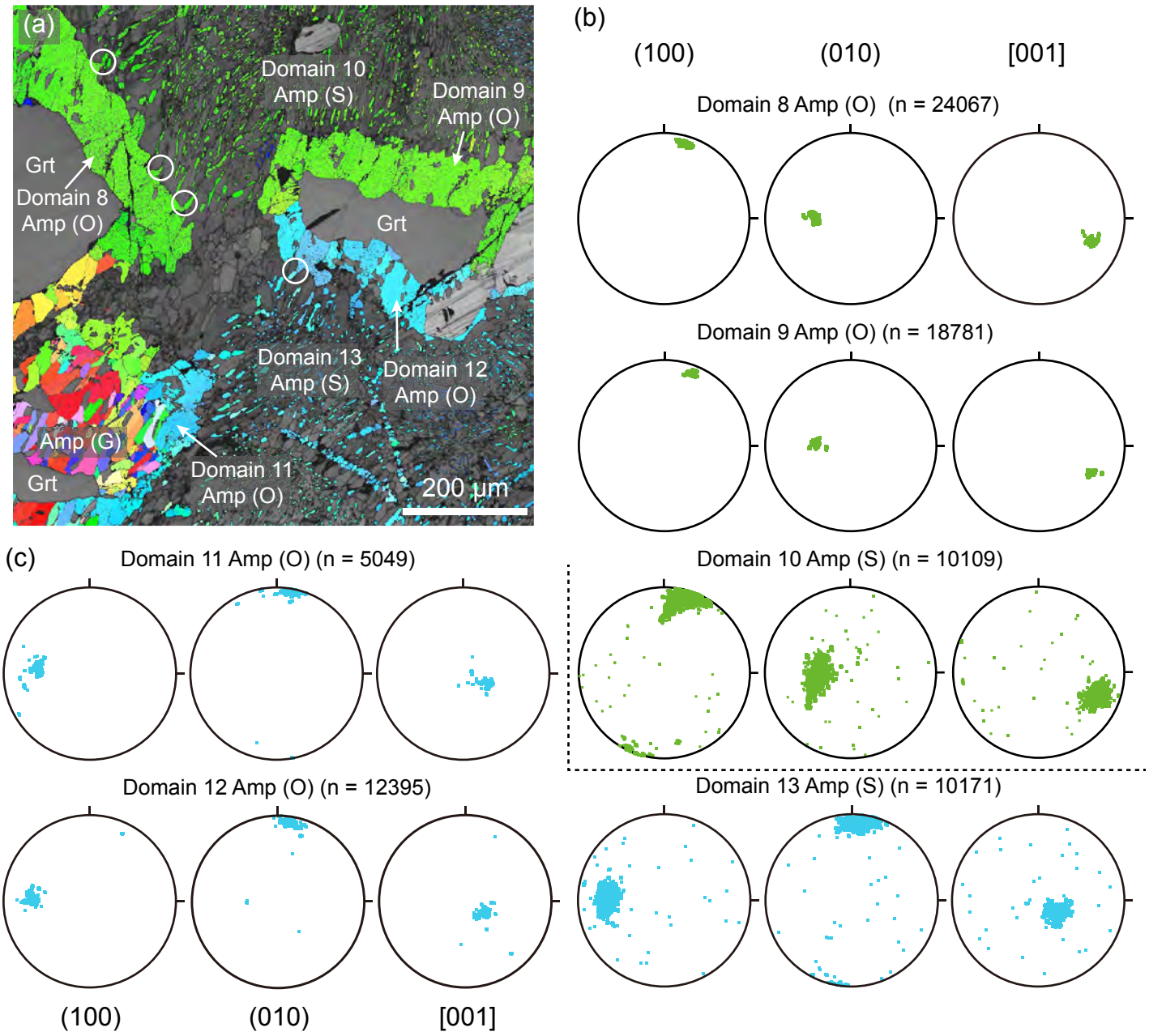

Figure 11. (a) Electron back-scattered diffraction (EBSD) pattern map (1 μm grid step) of Amp (O), Amp (G), and Amp (S) in an eclogite (91CH08) from the Donghai area, Sulu UHP metamorphic belt. Equal-area and lower hemisphere projection comparison of crystallographic orientations of the Amp (O) and Amp (S) segments in the sets of (b) domains 8, 9, and 10 and (c) domains 11, 12, and 13. Data n indicates the number of analysis points. Circles in (a) indicate a direct connection between Amp (O) and Amp (S).

Fig. 11 (Enami and others)

This is the peer-reviewed, final accepted version for American Mineralogist, published by the Mineralogical Society of America.
The published version is subject to change. Cite as Authors (Year) Title. American Mineralogist, in press.
DOI: https://doi.org/10.2138/am-2022-7996. http://www.minsocam.org/

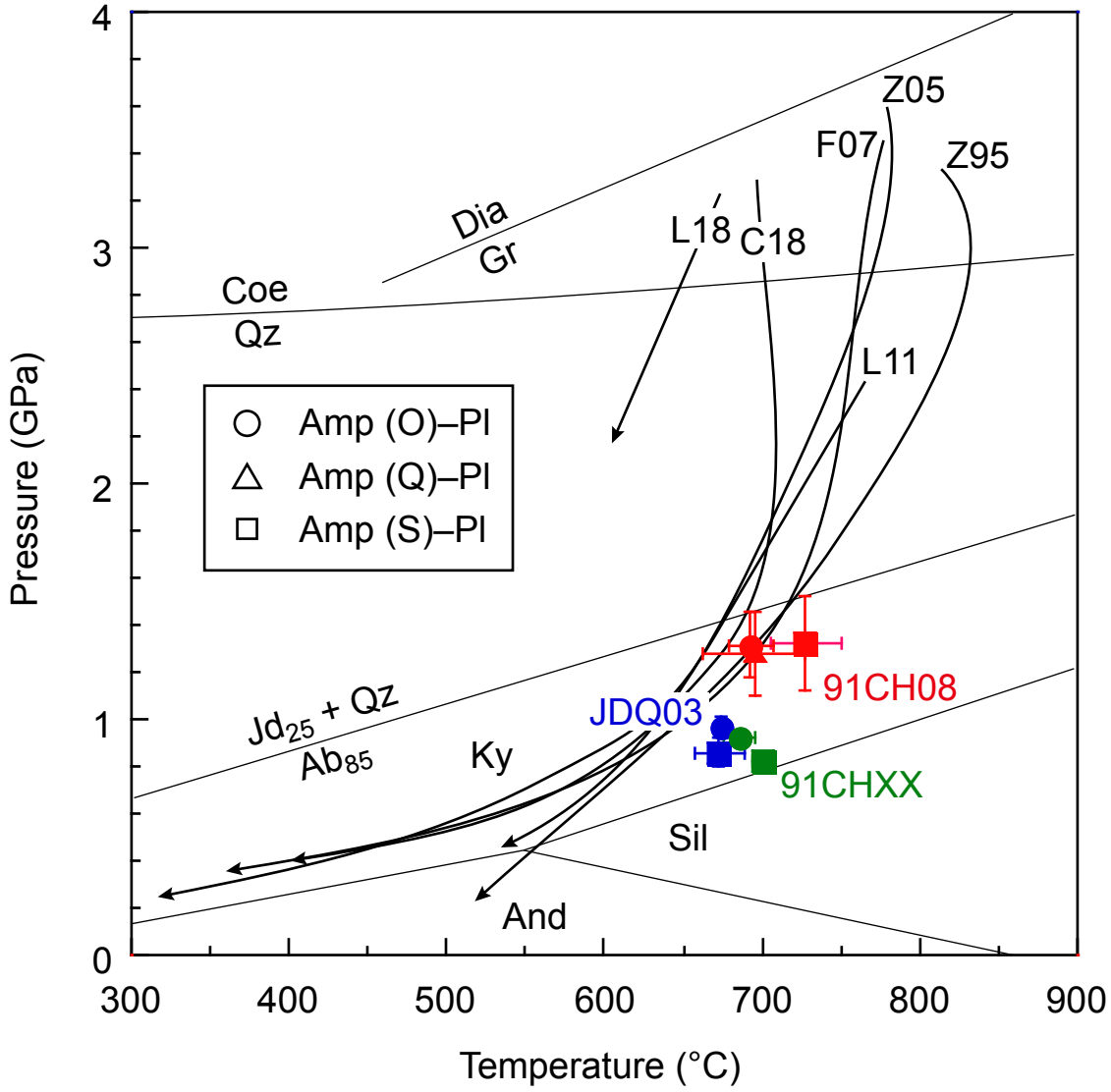

Figure 12. Comparison of the estimated equilibrium P-T conditions of aluminous calcium amphiboles + plagioclase (this study) and the exhumation P-T path of Donghai eclogites reported in literature. Abbreviations for references are: C18, Curetti et al. (2018); F07, Frezzotti et al. (2007); L11, Li et al. (2011); L18, Li et al. (2018); Z95, Zhang et al. (1995); Z05, Zhang et al. (2005). The univariant lines of Dia-Gr, Coe-Qz, Ab-Jd+Qz, and Al_2SiO_5 phases were caluculated using THERMOCALC software ver. 3.33 (Powell and Holland, 1988), internally consistent thermodynamic data set (Holland and Powell, 1998; updated June 2009), and program AX_2 (https://filedn.com/lU1GlyFhv3UuXg5E9dbnWFF/TJBHpages/ax.html).

Fig. 12 (Enami and others)

This is the peer-reviewed, final accepted version for American Mineralogist, published by the Mineralogical Society of America.
The published version is subject to change. Cite as Authors (Year) Title. American Mineralogist, in press.
DOI: https://doi.org/10.2138/am-2022-7996. http://www.minsocam.org/

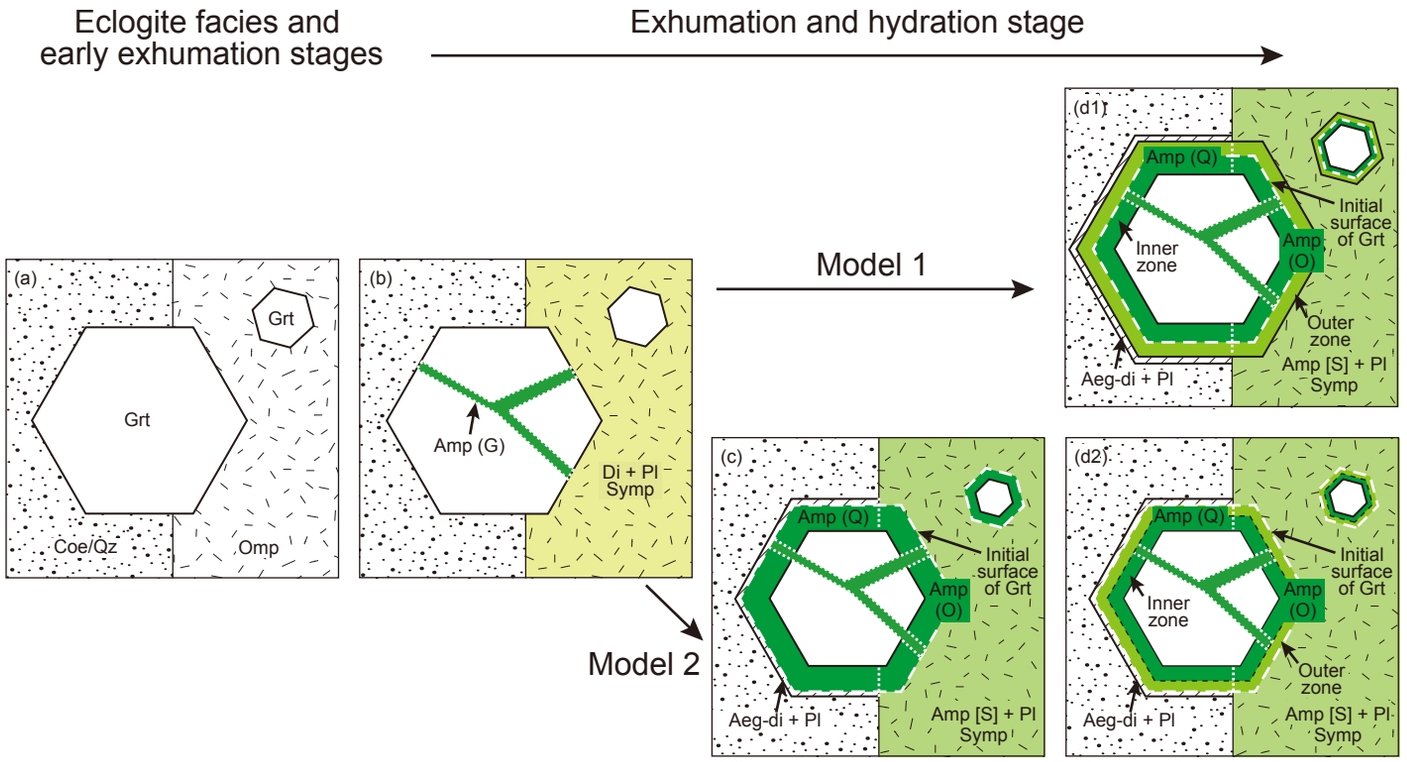

Figure 13. Conceptual diagram of growth scenarios (Models 1 and 2) of retrograde amphiboles in the Donghai eclogites, Sulu UHP metamorphic belt during the exhumation and hydration stage. (a) Eclogite facies and early exhumation stage. (b) Formations of sodic diopside + plagioclase symplectite and crack-filling amphibole [Amp (G)] at the early exhumation and hydration stage, although it is not clear which of these phenomena proceeded first, or if they were nearly simultaneous. (c) Formations of mantle amphibole around garnet [Amp (O) and Amp (Q)] and symplectitic amphibole [Amp (S)] (Model 2). (d1) Initial nucleation of amphibole at the interface between garnet and symplectite of sodic diopside + plagioclase, and subsequent growth of Amp (S) and Amp (O)/Amp (Q). The inner and outer zones of Amp (O) and Amp (Q) grew inward and outward from the initial surface of the garnet (dashed line), respectively (Model 1). (d2) The formation of the inner and outer zones of Amp (O) and Amp (Q) by modification of the chemical composition of their outer parts due to re-equilibration (Model 2).

Fig. 13 (Enami and others)

This is the peer-reviewed, final accepted version for American Mineralogist, published by the Mineralogical Society of America.
The published version is subject to change. Cite as Authors (Year) Title. American Mineralogist, in press.
DOI: https://doi.org/10.2138/am-2022-7996. http://www.minsocam.org/

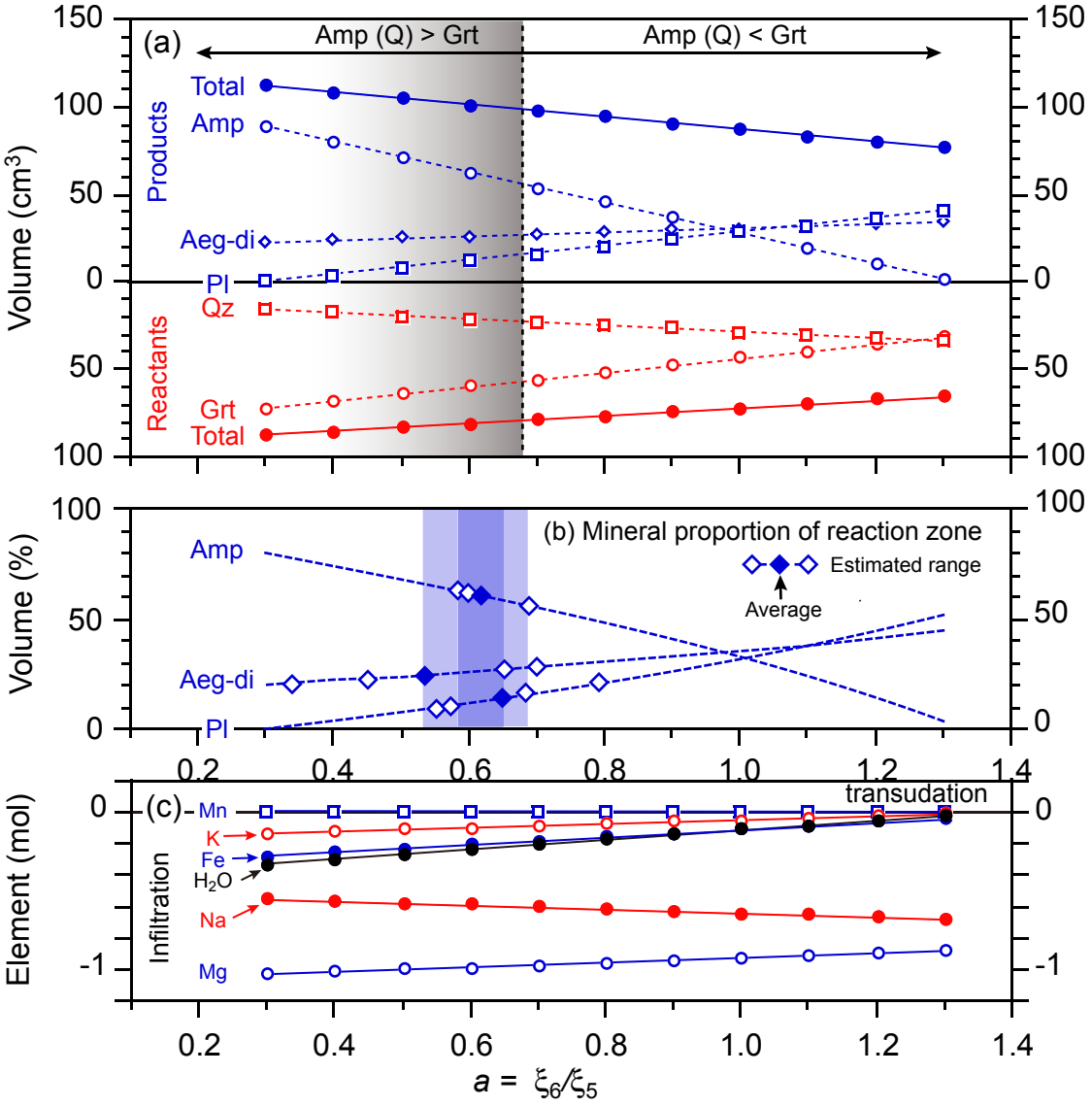

Figure 14. Volume change of minerals [(a) in cm^3 and (b) in %] based on the calculated stoichiometric coefficients of minerals as a function of $a = \xi_6/\xi_5$, where ξ_5 and ξ_6 represent the reaction extents of R5 and R6 in the text, respectively. The mineral volumes were estimated using the molar volumes listed in Table 3. The estimated volume proportions (%) of Amp (Q), aegirine-diopside, and plagioclase in the reaction zone are plotted in Fig. 14b for discussion on the possible range of the parameter *a*. (c) Stoichiometric coefficients of mobile components as a function of the parameter *a*.

Fig. 14 (Enami and others)